Modeling and Control of

McKibben Artificial Muscle Robot Actuators

by Bertrand Tondu and Pierre Lopez

Industrial robots are powerful, extremely accurate multijointed systems, but they are heavy and highly rigid because of their mechanical structure and motorization. Therefore, sharing the robot working space with its environment is problematic. Conversely, the human arm is not very accurate, but its lightness and joint flexibility due to the human musculature give it a natural capability for working in contact. The orientation of industrial robotics toward applications needing greater proximity between the robot and the human operator has recently led researchers to develop actuators sharing some analogies with natural skeletal muscle. This article describes the application of McKibben pneumatic artificial muscles to robotics. The McKibben pneumatic artificial muscle is undoubtedly the most promising artificial muscle for the actuation of new types of industrial robots.

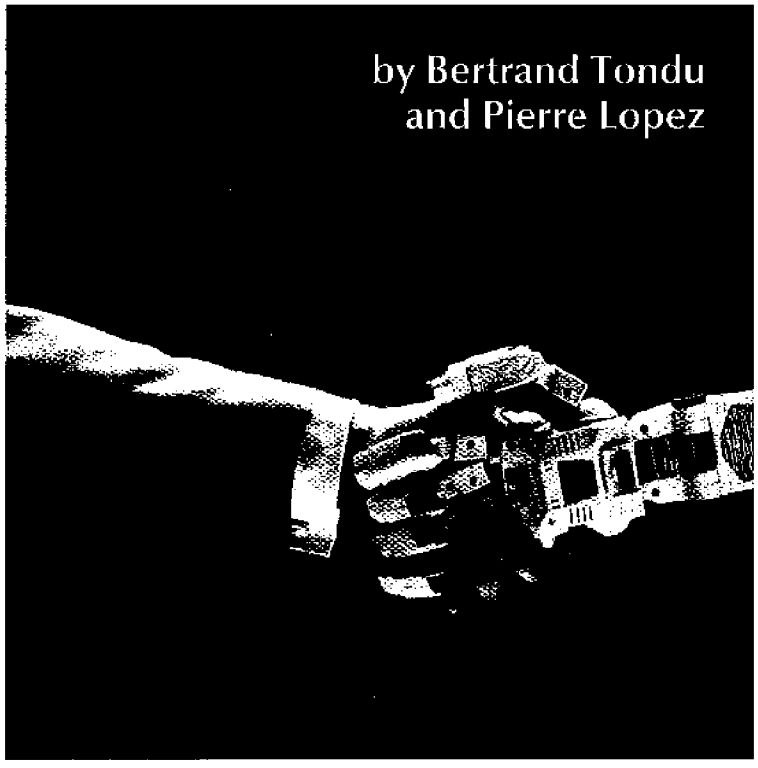

Tondu (tondu@insa-tlse.fr) and Lopez are with LESIA, Electrical and Computer Science Engineering Department, INSA, Campus de Rangueil, 31077 Toulouse, France.

1053-5888/00/$10.00©2000IEEE

The McKibben muscle was invented in the 1950s by physician Joseph L. McKibben to motorize pneumatic arm orthotics [1]-[4] to help control handicapped hands. The artificial muscle, which is simple in design, was made of a rubber inner tube covered with a shell braided according to helical weaving, as shown in Fig. 1(a). The muscle was closed by two ends, one being the air input and the other the force attachment point. When the inner tube was pressurized, the muscle inflated and contracted. The open-loop control of the artificial muscle by a simple pressure variation, as shown in Fig. 1(b), made this orthotic system very easy for those with disabilities to use. Although this pneumatic artificial muscle theme became rather active [5], [6], this actuator type was finally replaced in the 1960s by electric motors that do not need heavy and bulky pressurized gas tanks. Recently, there is renewed interest in that original actuation mode among industrial robotics researchers. In the 1980s, engineers of the Japanese tire manufacturer Bridgestone proposed a redesigned and more powerful version of the McKibben muscle called Rubbertuator (i.e., actuator in rubber [7], [8]) intended to motorize soft yet powerful robot arms. They are called Soft-Arms [9] and were commercialized by Bridgestone for painting applications [10]. Their application to assist disabled individuals [11] as well as to service robotics [12] has also been studied. Bridgestone's research has revived interest in studies on pneumatic artificial muscles. New types have been developed, such as the ROMAC (Robot Muscle Actuator) [13] or non-axial-contraction systems [14]-[16]. Due to its specific properties, however, the McKibben muscle seems to be the most suitable for applying the artificial muscle notion to robotics. Research and industrial teams working on the McKibben muscle prefer the original design or, like Bridgestone's engineers, introduce new versions of it such

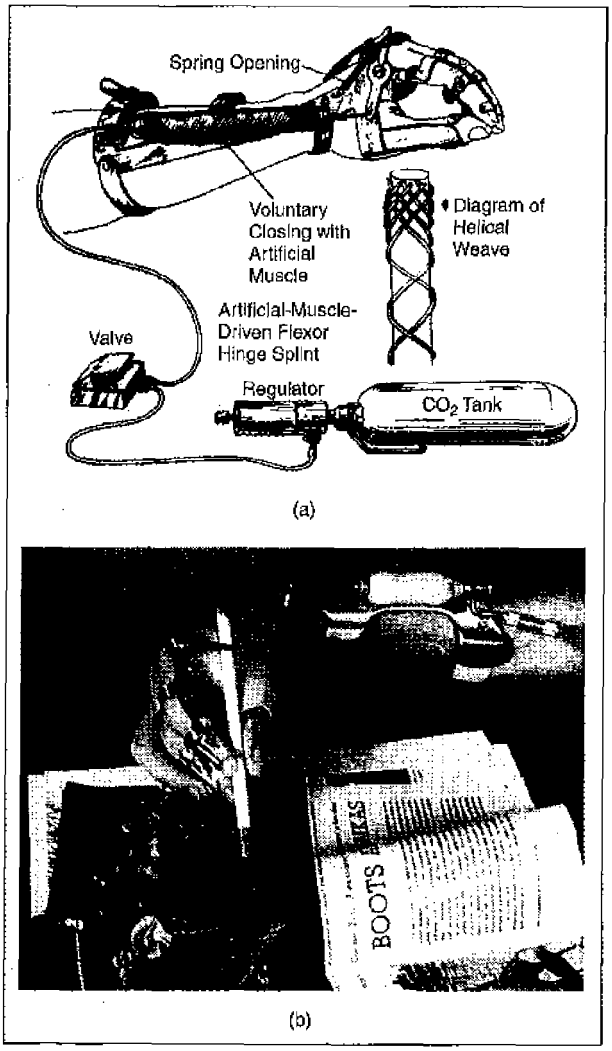

Figure 1. *Historical use of McKibben artificial muscle as arm orthotics to assist opening and closing the fingers of a handicapped hand: (a) McKibben muscle components (from [3]); (b) task example performed by a person with a disability with the assistance of the McKibben muscle (from [4]).*

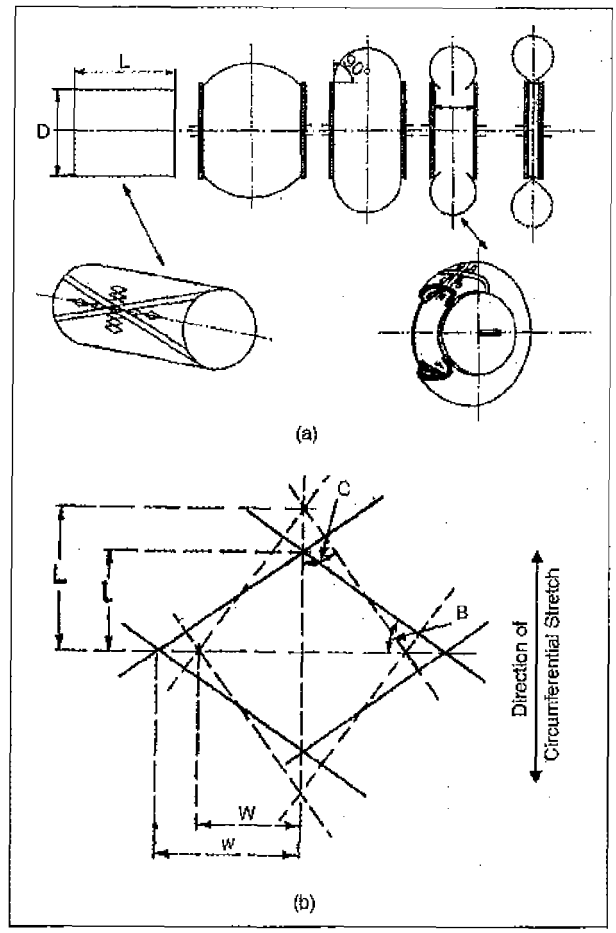

Figure 2. *Design of pneumatic tire carcases: (a) tire bending principle showing the double-helix weaving of the tire carcase (from [22]); (b) notion of bias angle (angle B of the figure) associated with the double-helix weaving of the tire carcase. (Reprinted with permission from the publisher [23].)*

as the Digit Muscle [17] or the SHADOW air muscle [18]. Thus, the McKibben artificial muscle looks like the archetype of artificial muscle, a topic that has attracted interest from robotics specialists as well as from neurophysiologists for experimental validation of nervous control system theories [19], [20]. For their part, pneumatic element manufacturers are attempting to derive benefit from the damped spring nature of the McKibben muscle (for example, the German manufacturer Festo, with its recent "Airtecture" inflatable building tensioned by "counterblowing muscles," which are obviously McKibben muscles [21]). Though new applications of the McKibben artificial muscle are expanding, its physics is still not widely known, and the control of actuators based on it is a topical issue.

This article starts by describing the working principle of the McKibben muscle. Static and dynamic modeling are then proposed, which notably takes into account the original friction model of the muscle thread. Next the fundamental model of the actuator, composed of two antagonistic McKibben muscles, is developed. The final section is devoted to control of the McKibben muscle actuator within the framework of variable-structure systems. This controller has been implemented on a two-degree-of-freedom (2-DOF) SCARA-type robot prototype motorized by McKibben muscle actuators.

Description and Working Principle of the McKibben Muscle

Due to its structure—a braided shell surrounding a rubber inner tube—the McKibben artificial muscle is like a pneumatic tire before bending. It is also interesting to consider the original McKibben description relative to classic treatises of pneumatic tire physics [22], [23] as illustrated in Fig. 2.

Contrary to a tire carcase weaving, however, the originality of the McKibben muscle lies in the use of a bias angle weak enough to allow inflation of the pressurized inner tube. This allows the textile shell to open when the inner tube inflates and then perform a true energetic transformation thanks to the elementary pantograph network formed by its helical weaving. By taking the cylindrical shape of the inner tube, this flexible pantograph network converts circumferential pressure forces into an axial contraction force, as shown in Fig. 3(a). This conversion principle is always valid when the muscle contracts because, due to the weaving symmetry, the artificial muscle maintains a globally cylindrical shape. This principle has led us to propose a basic parametrization of the McKibben muscle by means of the following three parameters, shown in Fig. 3(b).

- The initial braid angle, noted α_0, which corresponds to the notion of tire carcase bias angle, is defined as the angle between the muscle axis and each thread of the braided shell before its expansion. Consequently, this initial braid angle characterizes the elementary pantograph initial angle, and to geometrically characterize the weaving by this single parameter, we will assume that initially the textile shell entirely covers the rubber inner tube;
- The initial muscle length, denoted l_0, is defined as the active initial muscle length (i.e., the initial length of the muscle shell);
- The initial muscle radius, denoted r_0, is defined as the radius of the rubber inner tube assumed in contact with the braided shell. This definition involves considering a thin-wall inner tube (this point will be discussed later), and based on this hypothesis, the radius r_0 has been drawn in Fig. 3(b) as the initial internal radius of the muscle braided shell. Thus the full transmission of pressure to the braided shell can be assumed.

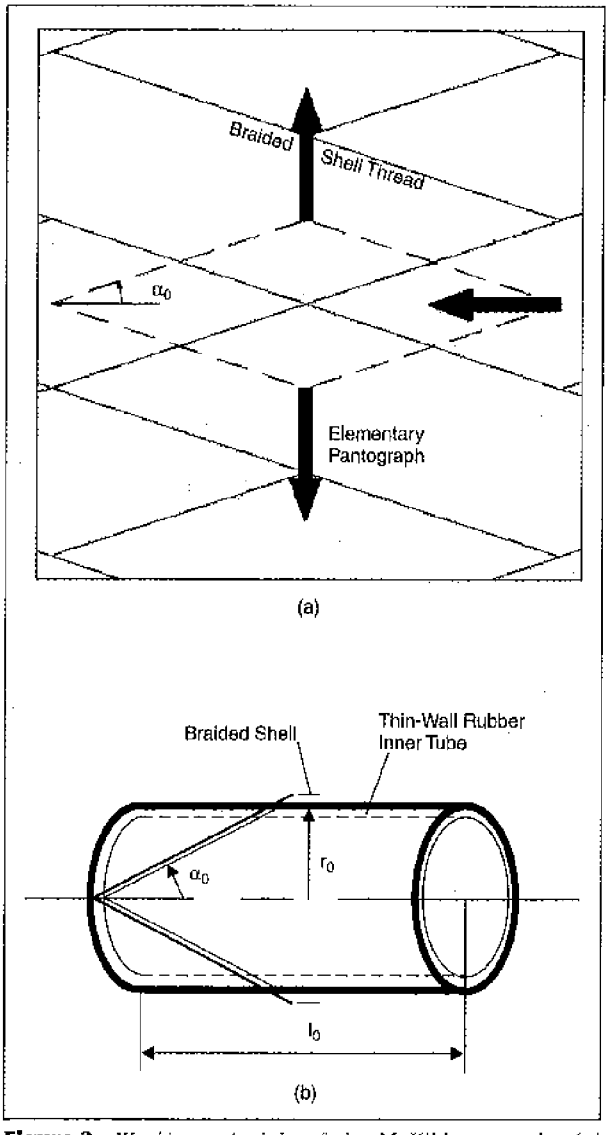

Figure 3. *Working principle of the McKibben muscle: (a) pressure force transformation principle by means of the pantograph network of the muscle braided shell; (b) basic geometrical parametrization of the artificial muscle.*

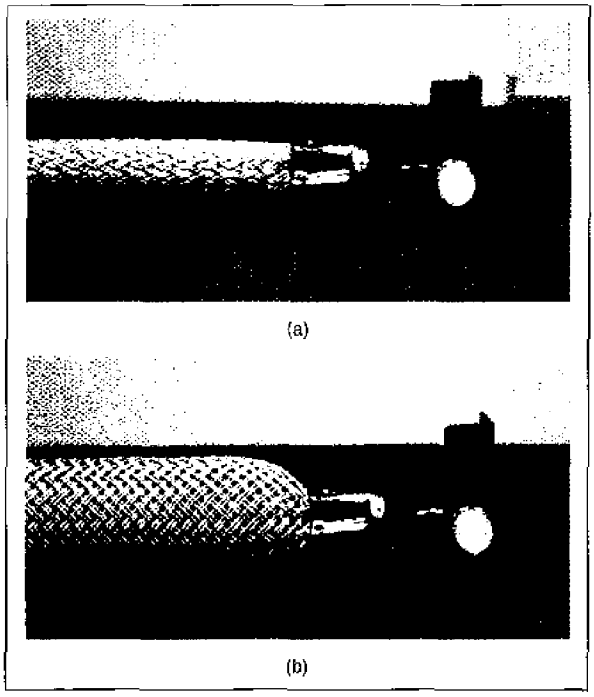

Figure 4. *Close-up of McKibben muscle designed at the laboratory; (a) initial contraction state; (b) maximum contraction state. This muscle geometrical parametrization is applied to the static McKibben muscle modeling described next, on which is based the dynamic modeling discussed later.*

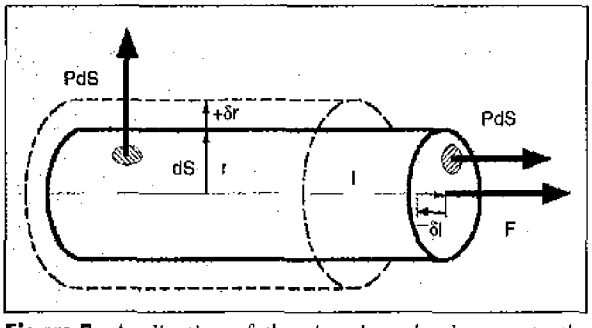

Figure 5. *Application of the virtual works theorem to the McKibben muscle static contraction analysis.*

This geometrical parametrization of the McKibben muscle does not take into account two important phenomena:

- The nonconservation of the cylindrical shape of the muscle, which takes a conic shape at its ends during contraction, as shown in Fig. 4. Modeling such a phenomenon is particularly complex because it depends on the weaving characteristics. Analysis of the McKibben muscle by means of finite elements, as currently developed at the University of Washington's Biorobotics Laboratory [24], could help model this phenomenon. As for us, we will consider an empirical side-effect coefficient (see the next section);
- The intrinsic mechanical aspects of the braided shell and the inner rubber tube. The braided shell is assumed to be unstrechtable, and we will ignore possible thread distortions that limit the artificial muscle contraction repeatability. The inner tube is assumed to be fully adapted to the working pressures of the muscle. Notably, the rubber tube radius and thickness are assumed to have been correctly chosen for the considered pressure field (see [25] for a discussion on this point).

Static Modeling of the McKibben Muscle

Basic Model of the Muscle Force Generator

Supposing that in a first stage the McKibben muscle keeps its cylindrical shape when it contracts, it is easy to determine the basic equation of its force generator by using the principle of virtual works. During contraction, the muscle radius, initially equal to r_0, becomes r and its length, initially equal to l_0, becomes l. If the static contraction force generated by the muscle is denoted F in absolute value, and if the positive axis for length variation is chosen in the muscle extension direction, the virtual work of the equilibrium force against the contraction force is $F\delta l$, where δl designates the elementary muscle length variation. The virtual work of pressure forces can then be expressed by considering an elementary volume variation δV, as done by Chou and Hannaford [26]

$$P\delta V = -F\delta l. \tag{1}$$

It is also possible, as we have proposed [25], to split the pressure forces into a lateral and an axial pressure. The virtual works theorem illustrated in Fig. 5 leads to

$$\begin{aligned}\delta W_{\text{lateral pressure}} + \delta W_{\text{axial pressure}} + \delta W_{\text{equilibrium force}} &= 0\\ \Rightarrow (2\pi rlP)(+\delta r) - (\pi r^2 P)(-\delta l) - F(-\delta l) &= 0.\end{aligned} \tag{2}$$

Therefore, the expression of the force F can be determined by considering the evolution of the muscle volume imposed by the braided shell. If α designates the current braid angle, the following relationships can immediately be deduced from the elementary pantograph opening principle:

$$\begin{aligned}(l/l_0) = \cos\alpha/\cos\alpha_0 \quad &\text{and} \quad r/r_0 = \sin\alpha/\sin\alpha_0\\ \Rightarrow r = r_0\left[\sqrt{1-\cos^2\alpha_0 (l/l_0)^2}/\sin\alpha_0\right].\end{aligned} \tag{3}$$

By applying these relationships and their derivatives to the virtual work equation, the following expression of F as a function of the control pressure P and the contraction ratio ε is deduced

$$\begin{cases} F(\varepsilon,P)=\left(\pi r_0^2\right)P\left[a(1-\varepsilon)^2-b\right],\ 0\le\varepsilon\le\varepsilon_{max} \\ \text{with}\ \ \varepsilon=(l_0-l)/l_0 \ \text{and} \\ a=3/\tan^2(\alpha_0),\quad b=1/\sin^2(\alpha_0). \end{cases} \tag{4}$$

This model brings to light a force evolution from an initial state at zero-contraction in which the produced force has a maximum value F_{max} to a maximum contraction state ε_{max} for which the force is zero. The corresponding expressions are

$$\begin{cases} F_{max}=\left(\pi r_0^2\right)P[a-b] & \text{for}\ \varepsilon=0 \\ \varepsilon_{max}=1-\sqrt{b}/a & \text{for}\ F=0. \end{cases} \tag{5}$$

This model is equivalent to the following one originally proposed by Schutle [2] and reconsidered by Chou and Hannaford [26]:

$$F(\alpha,P)=\left(\pi r_{90^\circ}^2\right)P\left[3\cos^2\alpha-1\right],\ \text{with}\ r_{90^\circ}=l_{thread}/n_{thread}\pi \tag{6}$$

where r_{90° designates the muscle radius for $\alpha=90$ deg—nonphysically reachable—which is in practice determined from l_{thread} representing the thread length and n_{thread} representing the number of turns of the thread. The equation (4) model parametrized in ε, however, seems better adapted for experimental validation than the model pararmetrized in α of (6). Moreover, the demonstration of the muscle force in the equa-

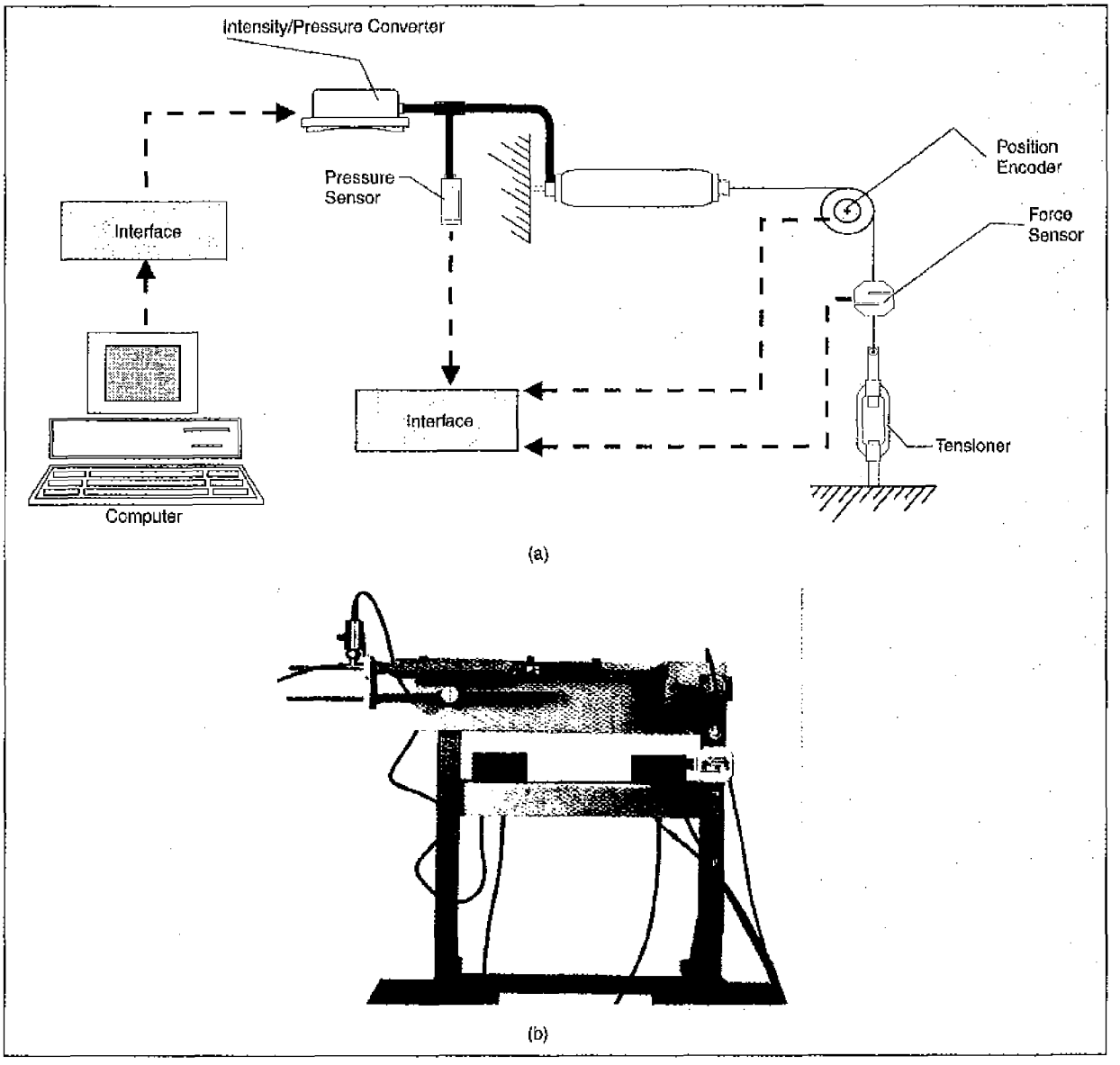

Figure 6. *Experimental setup for static analysis of the McKibben muscle performing an isometric contraction of the artificial muscle (i.e., at constant length): (a) setup components; (b) setup photograph.*

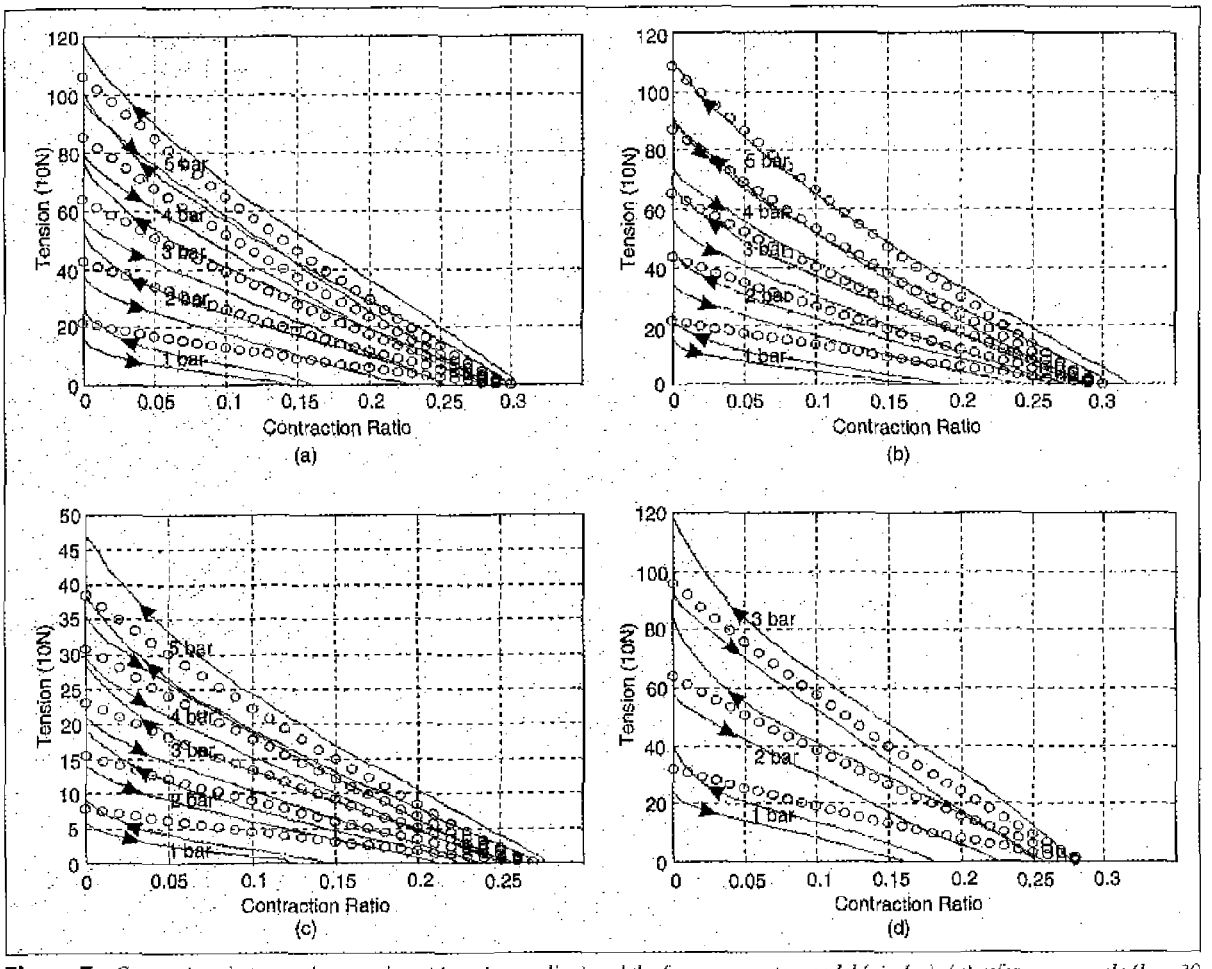

Figure 7. *Comparison between the experiment (continuous line) and the force generator model (circles): (a) reference muscle ($l_0 = 30$ cm, $r_0 = 0.7$ cm, $\alpha_0 = 20°$ with $k = 1.30$); (b) insensitivity to the initial muscle length ($l_0 = 15$ cm, $r_0 = 0.7$ cm, $\alpha_0 = 20°$ with $k = 1.30$); (c) effect of the initial braid angle ($l_0 = 30$ cm, $r_0 = 0.7$ cm, $\alpha_0 = 30°$ with $k = 1.25$); (d) effect of the initial muscle radius ($l_0 = 30$ cm, $r_0 = 0.85$ cm, $\alpha_0 = 20°$ with $k = 1.35$).*

tion (4) form leads to the proof of the Rubbertuator formula given in Bridgestone's technical reports and reported in works using Soft-Arms [8]-[10], [12], [37], [38]. The relationships of coefficients a and b that we have made explicit do not appear in Bridgestone's reports.

Before addressing the conflict between this theoretical model and the experiment, it is important to recall that the model reported here, as well as Chou and Hannaford's model, is based on the hypothesis of an infinitely thin inner tube. Thus, the muscle radius r is the internal braided shell radius. In practice, this hypothesis can be considered satisfied if the ratio between the tube thickness and the inner rubber tube is about 1:10 [27]. If the tube thickness exceeds this limit, it can no longer be assumed that pressure forces are fully transmitted to the braided shell. The global analysis by means of virtual works is no longer valid. Local analysis of the distributed forces within the pressurized inner tube would be necessary to determine the proportion of pressure transmitted to the shell. This point will not be discussed in this article; rather, we will consider a McKibben muscle equipped with a thin rubber tube, optimum as far as the pressure force conversion is concerned.

A disadvantage of the model is that its design is based on the hypothesis of a continuously cylindrical-shaped muscle, whereas it takes a conic shape at both ends when it contracts. Consequently, the more the muscle contracts, the more its active part decreases. This phenomenon results in the actual maximum contraction ratio theoretically being smaller than that expected from (5). To account for this side effect, a parameter $k (k \leq 1)$ is considered, which amplifies the contraction ratio ε by the factor k. The modified force generator model is

$$F(\varepsilon, P) = \left(\pi r_0^2\right) P\left[a(1 - k\varepsilon)^2 - b\right], \quad 0 \leq \varepsilon \leq \varepsilon_{max} \tag{7}$$

and the maximum contraction ratio is then divided by the factor k

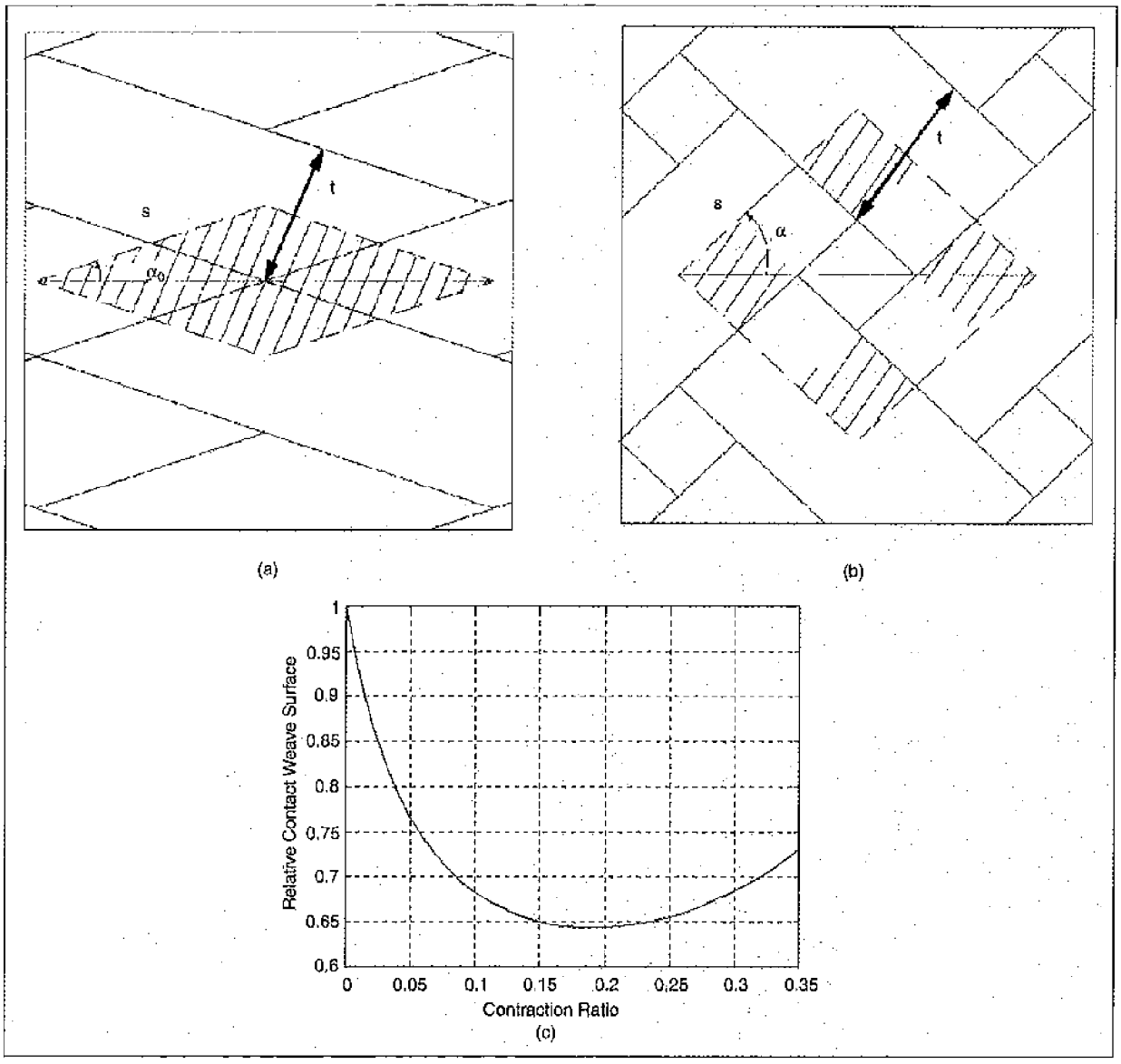

Figure 8. *Contact surface analysis of the McKibben muscle braided shell: (a) and (b) elementary surfaces definition; (c) simulated evolution of the ratio* $S_{\text{contact}} / (2\pi r_0 l_0)$.

$$\varepsilon_{\max} = (1/k)\left(1 - \sqrt{b/a}\right). \tag{8}$$

Inserted in this way within the considered static model, the parameter k does not modify the value of the maximum force given at zero contraction ratio. This is in concordance with the experiment since the muscle has a cylindrical shape only when its contraction ratio is zero [see Fig. 4(a)]. Furthermore, the parameter k allows adapting the model maximum contraction ratio given by (8) to the experimental data. Thus, it tunes the "slope" of the considered static model.

Two approaches have been considered for selecting the parameter k. In the first approach, a constant value of k has been estimated. For our muscles made of rayon braided threads (10 to 30 cm in initial length, 0.5 to 1 cm in initial radius, 20 to 30° in initial braid angle), a k parameter of 1.25 to 1.35 is relevant (k increases when initial radius increases or initial angle decreases). Fig. 7 shows the comparison between the experiment and the force model discussed above in the case of four muscles designed at the laboratory and tested on the experimental setup shown in Fig. 6. For a given pressure generated by an intensity/pressure converter (i.e., a servovalve generating a constant outlet pressure for a given input current) [28], the static muscle force is recorded. A tensioner is used to make the contracted muscle length variable. In this way, the static characteristics $F(\varepsilon, P)$ at constant pressure are obtained. In our experiments, the muscles have a rubber tube made of butyl of 50-shore hardness. At rest, the inner tube has a 10-mm internal diameter and a 0.6-mm thickness.

Experimental results validate the following properties of the McKibben muscle expressed in the force generator model considered:

1) Static force is globally proportional to muscle cross-sectional area (πr_0^2),

2) Static force is globally independent of initial length l_0,

3) Static force is globally proportional to control pressure P,

4) Maximum static force increases as the muscle initial braid angle α_0 decreases,

5) Static force decreases almost linearly with contraction ratio according to a slope globally proportional to control pressure P.

The McKibben pneumatic artificial muscle is undoubtedly the most promising artificial muscle for the actuation of new types of industrial robots.

It is interesting to note that the McKibben muscle shares the three first properties with the pneumatic cylinder. The second property is limited, however, by a specific side effect due to the crimping of the muscle tips. By the mere fact of the muscle design, the inner tube has at rest (i.e., at zero pressure) an external radius less than r_0. Consequently, in practice, the active length of the muscle under pressure, in its initial state (i.e., at zero contraction ratio), is l_0 if we neglect the minor side effect of the muscle crimping which imposes at muscle tips a radius a bit less than r_0. That is the reason the 15-cm-long muscle of Fig. 7(b) produces a maximum force about 10% less than the maximum force produced by our 30-cm-long reference muscle of Fig. 7(a). The fourth property highlights the importance of choosing the optimum initial braid angle to control the maximum force generated by the muscle. It also highlights the McKibben muscle's exceptional capability for a high maximum force-to-weight ratio (the mean weight of our muscles is about 50 g). The choice of a low initial braid angle, however, is limited by the rupture in extension of the rubber, since the lower the initial braid angle, the more the muscle radius increases. In practice, an initial braid angle of about 20° appears to be relevant, and, in this case, the size of the muscle varies satisfactorily during contraction since its radius almost doubles. The fifth property is the functional analogy property with skeletal natural muscle. The "natural compliance" notion of the antagonistic muscle actuator, which has been developed elsewhere [29] and justifies the joint "softness" of robot arms actuated by McKibben muscles, is based on this analogy.

The force model, including the constant parameter k, has enabled us to validate experimentally the basic static properties of the McKibben muscle; however, the model fails at low pressure. The behavior of the McKibben muscle at low pressure brings complex phenomena into play linked to the rubber elasticity of the inner tube as to the interaction between the braided shell and the inner tube. The accurate analysis of these phenomena is still to be done, and within the framework of this article, we will not deal with this difficult question. It is easy, however, to improve the considered static model by making k dependent on pressure P to bring the corresponding static characteristics at constant P closer to the experimental results. The following two-parameter relationship has been considered in which a_k and b_k are constants estimated for each muscle:

$$k = a_k e^{-P} + b_k. \tag{9}$$

Fig. 9 shows the comparison between the experiment and the new model for our reference muscle (l_0 = 30 cm, r_0 = 0.7 cm, α_0 = 20° with a_k = 3.55, b_k = 1.25) represented by circles. This modified model is now better located at the center of the hysteresis cycle of each static characteristic at constant pressure. It will be used to develop our analysis of the McKibben muscle dynamic contraction.

Consideration of a Friction Model

Because hysteresis corresponds to a greater generated force when the muscle extends (ε decreasing) compared with that generated when the muscle contracts (ε increasing), we believe this phenomenon is due to the thread-on-thread friction acting inside the muscle braided shell. Friction seems fundamental to understanding the McKibben muscle contraction, as we will see next. The working principle of the McKibben muscle implies that the fibers in contact with the inner tube stay rigidly locked with it during the contraction to fully transmit the pressure of the inner tube to the braided shell. Thus, theoretically, no friction has to be taken into account between the inner tube and the braided shell. In consequence, the friction analysis will deal only with the friction acting inside the braided shell. Here we will limit our analysis to the static part of the friction. The weaving involves an interlacing of the thread according to the basic scheme of Fig. 1. If we assume that no sliding occurs between the rubber tube and the shell, the pressure inside the inner tube is entirely transmitted to the shell and the thread-on-thread pressure is consequently the inflation muscle pressure P. Thus the following expression can be considered to model the static dry friction:

$$\left|F_{\text{static dry friction}}\right| = f_s S_{\text{contact}} P \tag{10}$$

where f_s is the thread-on-thread static dry fiction coefficient and S_{contact} is the contact surface. If, in the first stage of the

demonstration, we neglect the cylindrical shape of the shell thread to assume full contact between shell threads, we can determine the contact surface as the surface covered by the braided shell due to the double-helix weaving. This surface is initially (i.e., before muscle contraction begins) the lateral surface of the muscle ($2\pi r_0 l_0$). The pantograph network opens and the contact surface decreases when contraction begins. Its evolution can be determined by using the geometrical characteristics of the pantograph network structure of the braided shell illustrated in Fig. 8. The elementary hachured pantograph of Fig. 8(a) represents the elementary contact surface $S_{\text{elem init}} = 2s^2 \cos\alpha_0 \sin\alpha_0$, where s designates the constant side of the pantograph. During contraction, this elementary surface opens while keeping side s constant. The elementary contact surface becomes the new hachured surface shown in Fig. 8(b). By considering the thread thickness t bound to s by the equation $t = 2s\cos\alpha_0 \sin\alpha_0$ deduced from Fig. 8(a), the elementary surface of Fig. 8(b), $S_{\text{elem current}} = 2s^2 \cos^2\alpha_0 \sin^2\alpha_0 / \cos\alpha \sin\alpha$, can be determined. The total contact surface of the shell against itself, S_{contact}, is deduced from the proportion between these two surfaces. Having considered the muscle-specific evolution of the radius as a function of its length (3), we obtain

$$S_{\text{contact}} = (2\pi r_0 l_0)\frac{S_{\text{elem current}}}{S_{\text{elem init}}} = (2\pi r_0 l_0)\left(\frac{r_0}{r}\right)\left(\frac{l_0}{l}\right) = (2\pi r_0 l_0)\frac{\sin\alpha_0}{(1-\varepsilon)\sqrt{1-\cos^2\alpha_0(1-\varepsilon)^2}}. \quad (11)$$

Finally $(1-\varepsilon)$ is changed into $(1-k\varepsilon)$ to equate the contact surface analysis with the force-productive analysis. Fig. 8(c) gives, in the case of our reference muscle ($l_0 = 30$ cm, $r_0 = 0.7$ cm, $\alpha_0 = 20°$ with $k = 1.30$), the simulated evolution of the ratio between the contact surface and its initial value as a function of the contraction ratio.

Using this contact surface model, we can estimate the friction coefficient from the recording of the static muscle force [Fig. 7(a)]. The resulting model, shown in Fig. 9, now takes the static hysteresis cycle into account relatively well. It has been obtained with an estimated friction coefficient of 0.015. Such a static dry friction is in fact very low. According to the *Fibres, Plastics, and Rubbers Handbook* [30], the static dry friction coefficient of viscose rayon on viscose is about 0.2. Therefore, we must assume that only (1/13) of the textile shell surface is in contact with itself, which appears to be a reasonable assumption in accordance with the shell thread cylindrical nature. If we call $(1/n)$ the estimated ratio of the muscle lateral surface rubbing against itself, the static friction model considered will finally be

$$\left|F_{\text{static dry friction}}\right| = f_s(1/n)S_{\text{contact}}P. \quad (12)$$

The dynamic McKibben muscle analysis extends this static friction analysis.

Dynamic Modeling of the McKibben Muscle

The dynamic contraction of the McKibben muscle has been studied using the experimental apparatus shown in Fig. 10. This apparatus allows the muscle to lift a given load by means of a pulley when it contracts. An encoder mounted on the pulley axis gives the current muscle length. A special force sensor has been designed; light and compact, it is directly fixed to the muscle end to record the current force produced by the muscle during contraction. Initially, the load lies on a base and, in response to a numerical signal translated into pressure by means of the intensity/pressure converter, the muscle contracts until it reaches its equilibrium position [Fig. 10(b)]. This apparatus performs the isotonic contraction of the muscle lifting the load m. In the experiments reported below, control pressure, muscle force, and linear muscle contraction in the form of position x, with x being defined as $(l_0 - l)$ [Fig. 10(a)], are simultaneously recorded. The isotonic contraction proves that the

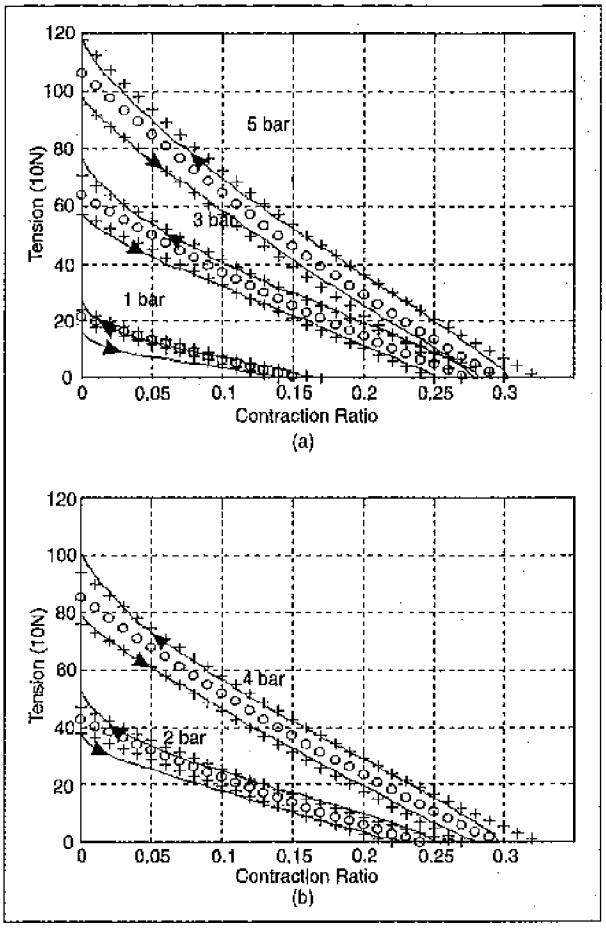

Figure 9. *Comparison between experiment results (continuous line) and the force generator model using the dependence relationship between k and P, without friction model (circles) and including the static dry friction model (crosses): (a) cases of P = 1,3,5 bar; (b) cases of P = 2,4 bar.*

natural damping of the McKibben muscle is very similar to skeletal muscle behavior. A simple and general model for the dynamic dry friction coefficient f can be considered in the form of the following three-parameter relationship:

$$f = f_k + (f_s - f_k)e^{-(\dot{x}/\dot{x}_s)}. \tag{13}$$

Here f_s represents the static dry coefficient considered previously, f_k the maximum kinetic dry coefficient, and $\dot{x}_s$ a velocity constant between f_s and f_k. In the case of solids, f_k is generally smaller than f_s. In the case of a textile shell rubbing against itself, our experimental results have shown f_k is greater than f_s. That is why we have represented our considered friction model on Fig. 11(a) according to this situation. Its originality compared with typical solid friction models [31] emphasizes the McKibben muscle's originality. Higher kinetic friction due to hydrodynamic phenomena is typical of textile thread physics, as illustrated in Fig. 11(b), and is related to the friction of lubricated rayon threads (synthetic textile threads are indeed generally lubricated during their manufacture) [32].

As the experiments clearly show, however, the estimated kinetic muscle shell friction coefficient is still higher than the one produced by rayon physics; an approximate ratio of seven between the kinetic friction coefficient and the static one will be considered. To explain this phenomenon, we have considered the global behavior of the shell; the interlacing of the threads in motion seems to play the part of a rough surface in friction theory. Finally, the complete dynamic McKibben muscle force model, denoted F_{dyn}, where F designates the static expression of (7), will be

$$F_{dyn} = F - f(1/n)S_{contact}P\,\mathrm{sign}(\dot{x}). \tag{14}$$

The isotonic contraction performed using the Fig. 10 experimental apparatus can be written in the equation system shown below, where t_{lim} divides the two stages of the experimental isotonic contraction

$$\begin{cases} F_{dyn} = m\ddot{x}, & 0 \le t < t_{lim} \\ F_{dyn} - mg = m\ddot{x}, & t \ge t_{lim}. \end{cases} \tag{15}$$

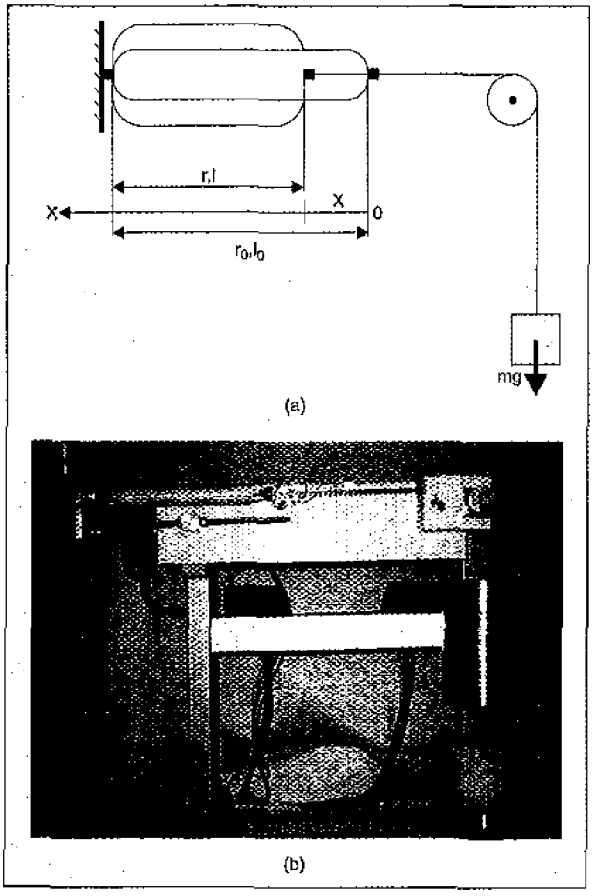

Figure 10. *Dynamic analysis of the McKibben muscle in isotonic contraction (i.e., at constant load): (a) illustration of principle; (b) corresponding experimental setup.*

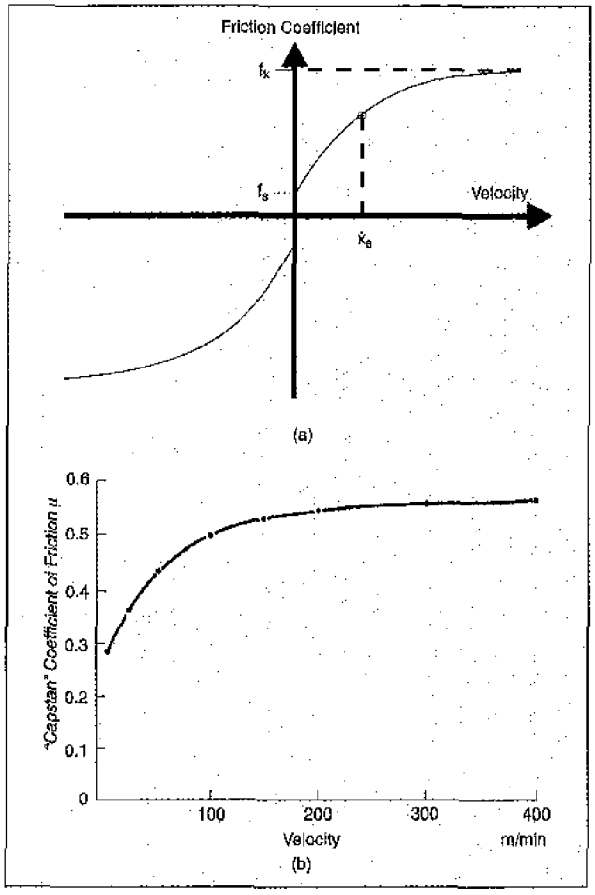

Figure 11. *Considered friction model for the McKibben muscle shell: (a) three-parameter friction mode; (b) typical variation of the friction coefficient with speed for rayon thread (from [32, p. 69]).*

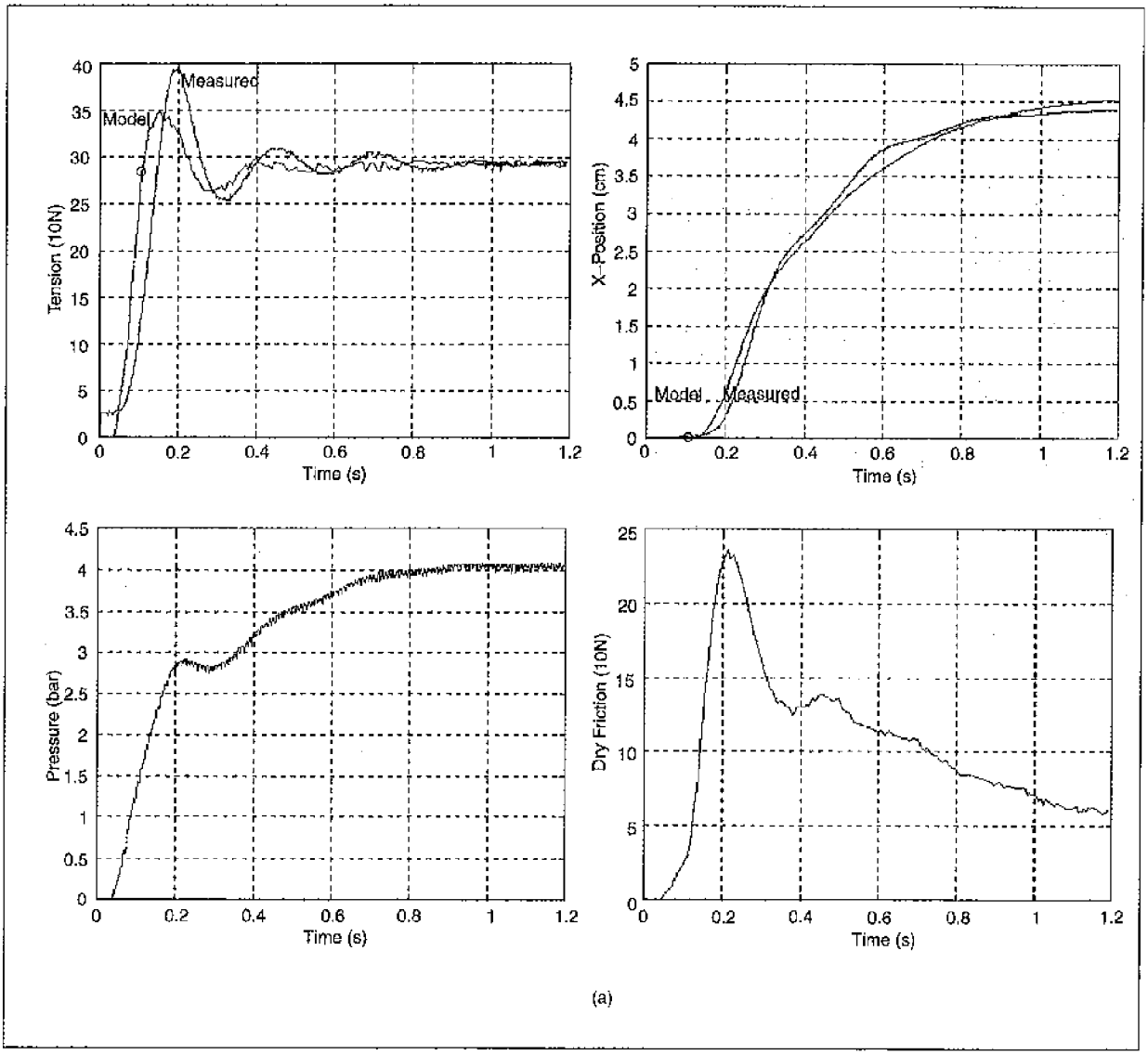

Figure 12. *Comparison between experiment and dynamic model in the case of our reference muscle (l_0 = 30 cm, r_0 = 0.7 cm, α_0 = 20°); (a) force and position evolution with corresponding actual pressure evolution and model dry friction evolution for P = 4 bar and m = 30 kg.*

Note that the load can be lifted only after time t_{lift}, when the muscle pressure has increased from zero to a value high enough to produce sufficient force to the load. This equation system can be solved using the MATLAB software Runge-Kutta procedure. The recording of the pressure has been directly used for generating a very accurate linearly interpolated pressure model. Fig. 12 presents examples of results obtained in three different situations of pressure and load: m = 30 kg and P = 4 bar, m = 20 kg and P = 3 bar, m = 10 kg and P = 2 bar. In all the experiments, the following parameter values have been chosen: $f_s / n = 0.015$, $f_k / n = 0.105$ (it follows that f_k / f_s is 7), and $\dot{x}_s$ = 0.15 m/s. The two dynamic parameters f_k and $\dot{x}_s$ have been adjusted using the force recording on successive trials so that $\dot{x}_s$ gives the slope between successive force extrema and f_k gives the force extremum value. The values lead to good concordance between experiment and theory for the muscle force shape. The resulting concordance is good for the muscle contraction; it is not as good, however, when the motion starts at very low pressure [Fig. 12(c)], for which the force generator model is still limited [see Fig. 9(a)].

Other experiments performed for different pressures and loads have confirmed the global validity of the proposed model for the set of parameters considered. This model finally appears to be more relevant than the one we have attempted to build from a friction representation in the form of a viscous linear term [33].

This dynamic model highlights the McKibben muscle dynamic properties:

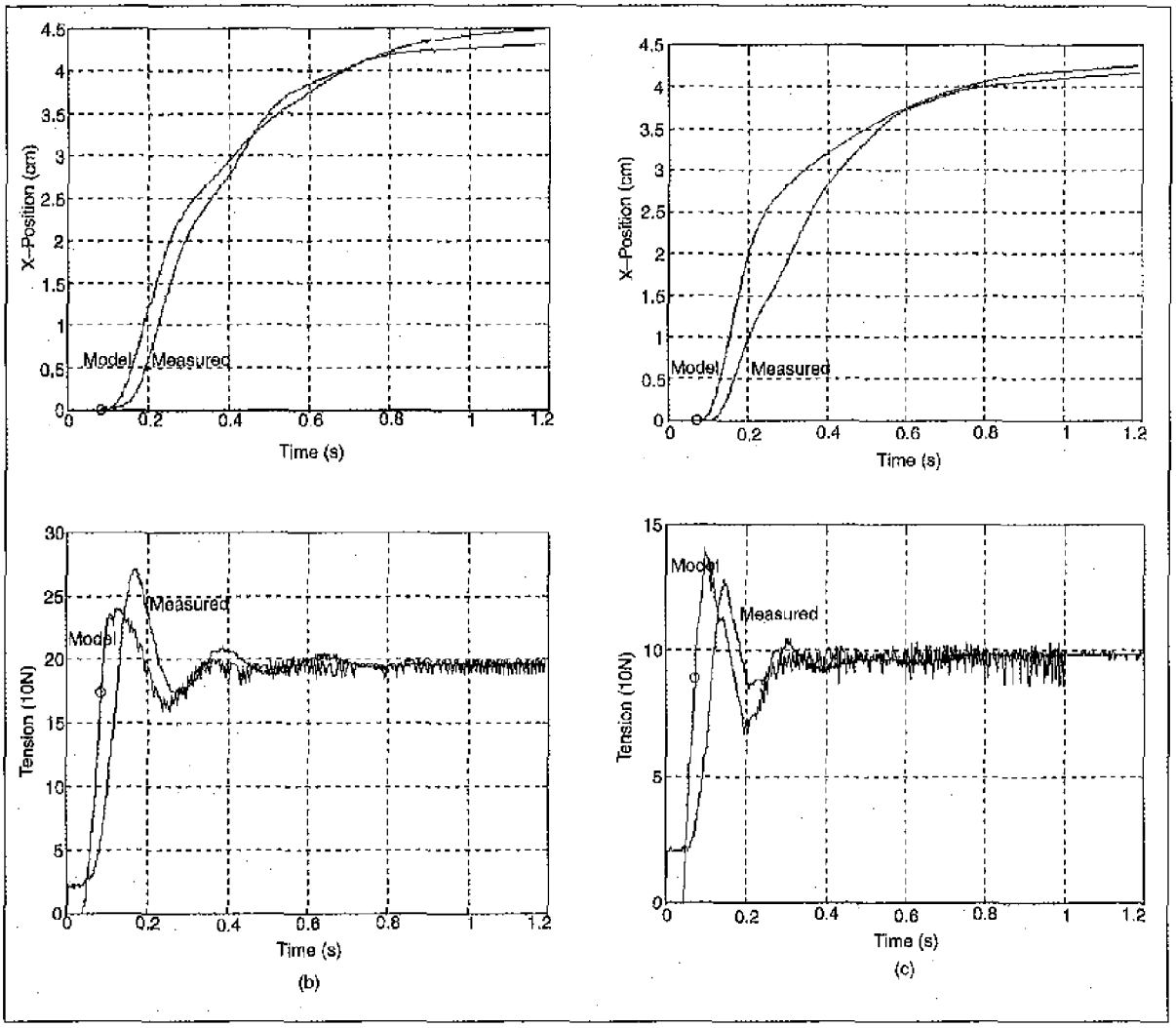

Figure 12. *Comparison between experiment and dynamic model in the case of our reference muscle (l_0 = 30 cm, r_0 = 0.7 cm, α_0 = 20°); (b) force and position evolution for P = 3 bar and m = 20 kg; (c) force and position evolution for P = 2 bar and m = 10 kg (the circle represents the motion beginning according to the model).*

1) The McKibben muscle contraction is naturally damped by nonlinear kinetic friction inherent to its braided shell;

2) The McKibben muscle contraction time is some tenths of a second.

These two dynamic properties, in analogy with natural skeletal muscle dynamic performances, complement the five static McKibben muscle properties given previously.

Actuator Made of Two Antagonistic McKibben Muscles

Working Principle of the Actuator

Two McKibben muscles put into antagonism define a rotoid actuator based on the physiological model of the biceps-triceps system. The two muscles are connected by means of a chain driving a sprocket. The force difference between the agonist and the antagonist generates a positive or negative torque; however, unlike natural skeletal muscle, the McKibben artificial muscle has no passive tension due to the braided shell inextensibility. Both muscles must be inflated at the same pressure P_0 and have the same contraction ratio ε_0 in the initial state to keep the actuator in good working order. When the agonist is inflated at pressure P_1 different from the antagonist pressure P_2, an actuator rotation of angle θ is produced, whereas the sum of the two contraction ratios (denoted ε_1 and ε_2, respectively) is equal to $2\varepsilon_0$. This principle is illustrated in Fig. 13.

From this working principle, a model of the torque T produced by the actuator can be built, based on the static force

generator model of (7). The agonist force will be denoted F_1, the antagonist force F_2, and the sprocket radius R. We obtain

$$\begin{cases} T = R(F_1(\varepsilon_1, P_1) - F_2(\varepsilon_2, P_2)), \text{ with} \\ \varepsilon_1 = \varepsilon_0 + R\theta / l_0, \varepsilon_2 = \varepsilon_0 - R\theta / l_0. \end{cases} \quad (16)$$

If we consider only the case of constant parameter k, the expression above can be developed in the following form:

$$\begin{cases} T = (P_1 - P_2)(K_1 + K'_1\theta^2) - (P_1 + P_2)K_2\theta, \text{ with} \\ K_1 = (\pi r_0^2)R[a(1 - k\varepsilon_0)^2 - b] \\ K'_1 = (\pi r_0^2)Ra(kR / l_0)^2 \\ K_2 = (\pi r_0^2)R2a(1 - k\varepsilon_0)kR / l_0. \end{cases} \quad (17)$$

A disadvantage of the model is that its design is based on the hypothesis of a continuously cylindrical-shaped muscle, whereas it takes a conic shape at both ends when it contracts.

The case of constant parameter k has been privileged compared to the case of k as a function of P because it leads to this basic expression of the torque produced by the actuator from which the fundamental actuator properties can be derived. Because this model overestimates the force at low pressure, however, it overestimates the antagonistic force F_2, which leads to a value of the torque given by the model weaker than the actual one. This will be illustrated in Fig. 15, showing the slope of the static gain from the actuator model being slightly lower than the slope of the actual static characteristic.

When choosing the initial braid angle in the range [15°-30°], and noting that ε_0 is limited to $1/2\varepsilon_{max}$, which in practice means within the range [0.1-0.15], we can easily demonstrate that the additive term in $K'_1\theta^2$ is a negligible quantity against the term K_1 to within about 5%. The simplified torque model is deduced as

$$T = K_1(P_1 - P_2) - K_2(P_1 + P_2)\theta. \quad (18)$$

This expression makes it possible to distinguish a motor term, strictly speaking, proportional to $(P_1 - P_2)$, from a restoring term of spiral spring type proportional to θ, and for which stiffness can vary proportionally to $(P_1 + P_2)$. It is to be compared with the physiological models of the torque produced by the biceps-triceps system, such as the one built by N. Hogan from a linear approximation of the length-tension characteristics of a cat muscle (Fig. 14) [34]

$$T = T_{max}(u_b - u_t) - K(u_b + u_t)\theta \quad (19)$$

where u_b and u_t represent the normalized nervous controls of the biceps and triceps, respectively, and T_{max} and K are two constants.

Thus our model looks like the analogical form of N. Hogan's biological model [34] in which the pressure vari-

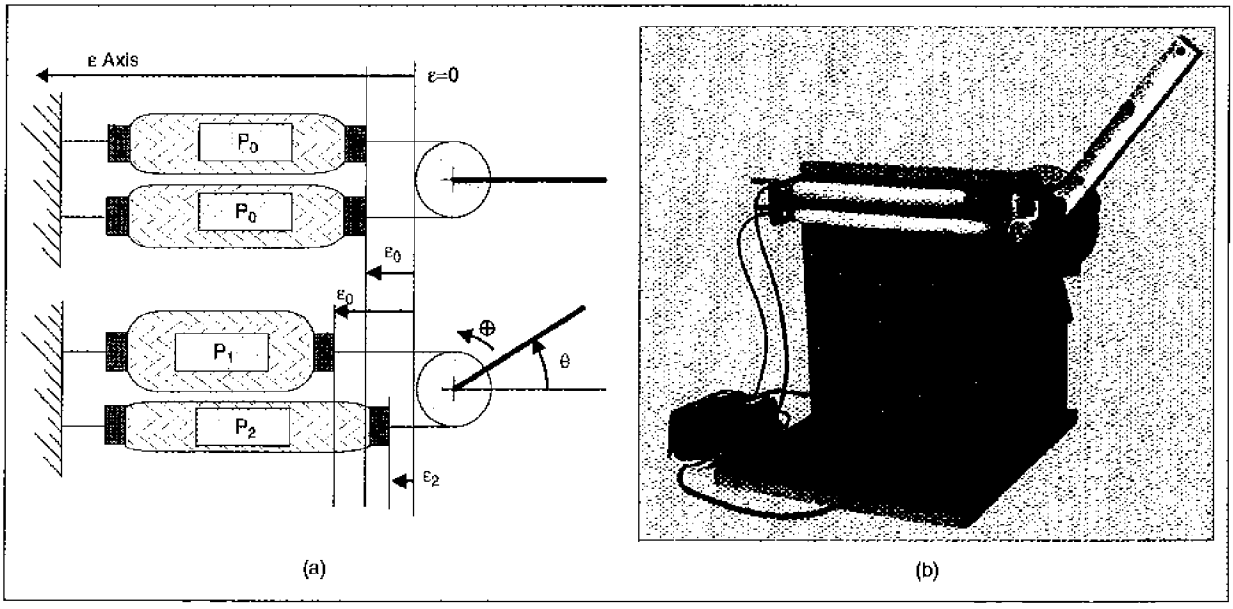

Figure 13. *Antagonistic McKibben muscle actuator: (a) working principle; (b) experimental setup.*

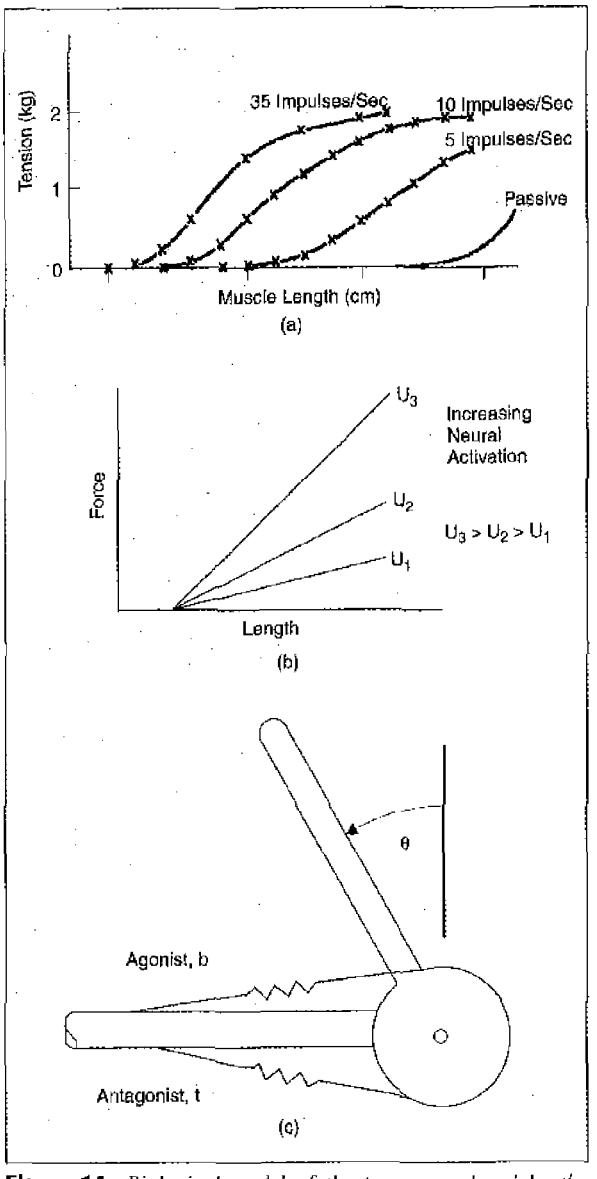

Figure 14. *Biological model of the torque produced by the biceps-triceps system (from [34]): (a) actual characteristics of a cat soleus muscle considered by the author; (b) linear approximation of the actual characteristics; (c) modeling of the biceps-triceps antagonistic system.*

ables play the part of biceps and triceps nervous controls. This comparison highlights the singularly anthropomorphic feature of the antagonistic McKibben muscle actuator, which we will express later using the natural compliance notion.

Monovariable Approach for the McKibben Muscle Actuator Control

A monovariable approach of the McKibben muscle actuator, which could be called symmetrical co-contraction by analogy with the neurophysiological terminology [35], is now considered. The symmetrical pressure variation, applied from initial pressure P_0 in both muscles, will be noted ΔP. It leads to a single-input $\Delta(P)$, single-output (θ) control that makes it easy to adapt classic controllers to the actuator. By putting $P_1 = P_0 + \Delta P$ and $P_2 = P_0 - \Delta P$ in (18) above, the torque-model of the actuator becomes

$$T = 2K_1\Delta P - 2K_2 P_0\theta \tag{20}$$

which can be written in the following form:

$$\begin{cases} T = k_1\Delta P - k_2\theta, \text{with} \\ k_1 = 2K_1 \text{ and } k_2 = 2K_2 P_0. \end{cases} \tag{21}$$

This static model highlights the main originality of the actuator. Thanks to the constant-stiffness restoring torque, the actuator is very easily controllable in open loop. From (21), the following static relationship is deduced in which G represents the open-loop gain

$$\begin{cases} \theta = G\Delta P, \text{with} \\ G = \dfrac{K_1}{K_2} = \dfrac{l_0\left[a(1-k\varepsilon_0)^2 - b\right]}{2akR(1-k\varepsilon_0)P_0}. \end{cases} \tag{22}$$

This static gain expression has been verified experimentally, as shown in Fig. 15, which compares the theoretical model to the actual characteristics of the actuator used on our SCARA robot (see the next page) for which the parameters are as follows: $\alpha_0 = 23°$, $l_0 = 34$ cm, $r_0 = 0.7$ cm, $k = 1.25$, $R = 1.5$ cm, $P_0 = 2.5$ bar, $\varepsilon_0 = 0.1$. The actual hysteresis characteristic is a direct consequence of the braided shell friction against itself, which we have already analyzed.

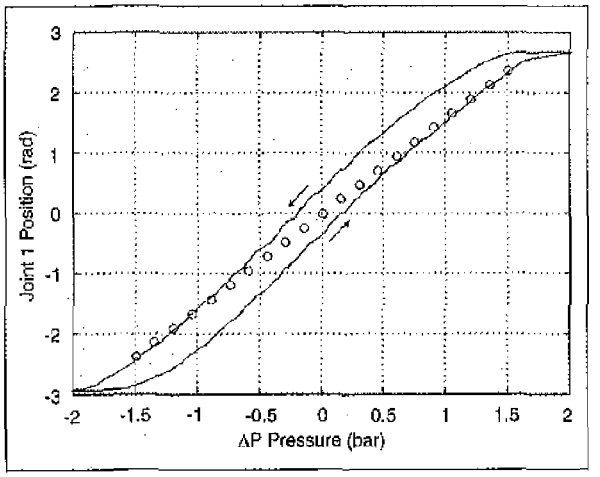

Figure 15. *Comparison between the static gain issued from the actuator model (circles) and the actual actuator characteristics (continuous line).*

Furthermore, when the actuator has been positioned at angle 0 by means of the pressure control ΔP and deviated from this equilibrium position by an angle variation $\delta\theta$, as illustrated in Fig. 16(a), the restoring torque generated is

$$\begin{cases} T_r = k_1\Delta P - k_2(\theta + \delta 0) = -k_2\delta\theta, & \text{since} \\ k_1\Delta P - k_2\theta = 0. \end{cases} \tag{23}$$

This equation expresses the natural stiffness of the actuator, which in the open-loop equilibrium position behaves like a spiral spring of stiffness k_2, as shown in Fig. 16(b).

We propose to call "natural compliance" the passive compliance quality given to the robot joint by the McKibben muscle actuator, by analogy with the passive compliance of our joints. It has promise in robotics because it extends the passive or active compliance limited to the wrist to other robot joints. It can be applied to service robotics involving contact between the robot arm and its environment. Two conditions are necessary to keep the robot in good working order. First, direct drive is required to maintain the actuator compliance. This constraint will be satisfied by means of the actuator power. Second, the closed-loop control of the actuator induces additional stiffness that has to be mastered. If we assume that the joint has been positioned at angle 0 by the control pressure ΔP, and if the joint is deviated $\delta\theta$ from the equilibrium position, the closed-loop control generates a pressure variation of $(-\delta P_{\text{C.L.}})$ by reaction. The equation of the restoring torque is now

$$T_r = k_1(\Delta P - \delta P_{\text{C.L.}}) - k_2(\theta + \delta 0) = -k_1\delta P_{\text{C.L.}} - k_2\delta\theta. \tag{24}$$

Consequently, the restoring torque is increased in absolute value by the term $k_1|\delta P_{\text{C.L.}}|$, which can take a value significantly exceeding that of the term $k_2|\delta\theta|$. For example, the presence of a nonmastered integrator in the closed loop can notably lead to a quick growth of the restoring torque, which causes a brutal backward motion.

This natural compliance would be of no practical utility, however, if the actuator had no natural damping. As can be seen in Fig. 17, which shows the dynamic actuator response (continuous line) of joint 1 and joint 2 of our SCARA-type robot (Fig. 18), the actuator damps naturally. To better understand this phenomenon, we have identified a linear model of the actuator in open loop. From a pressure variation numerical step ΔU corresponding to the physical pressure variation ΔP, we have shown by means of MATLAB software that it is possible to approximate the actuator constituted by the chain "I/P converter-McKibben muscle actuator-inertial load" by a second-order system

$$\theta(p) = \frac{b}{p^2 + a_1 p + a_2}\Delta U(p). \tag{25}$$

Fig. 17 gives the result of the identification for both axes of our SCARA robot. This result will be used directly in the control of our 2-DOF robot arm (described below).

Note that the intensity/pressure (I/P) converters have a quick dynamic response compared to the McKibben muscle dynamic contraction. Therefore, the viscous term is really specific to the McKibben muscle actuator. By considering the friction analysis developed earlier, we are able to interpret the presence of this viscous term as the approximation of the kinetic friction growing with speed. The correlation between natural damping and kinetic friction is proved by the identification of joint 2 compared to joint 1 identification. With the same actuator as joint 1, joint 2 drives a weaker inertial load than joint 1 and is thus more sensitive to nonlinear friction.

Adaptation of the McKibben Muscle Actuator to Robot Structures

The previous analysis has brought to light the close analogy between the McKibben muscle actuator and the skeletal muscular system based on natural compliance. The high maximum force-to-weight and force-to-volume ratios of the McKibben muscle lead to a feasible adaptation of the antagonistic McKibben muscle actuator to robot arms. When the

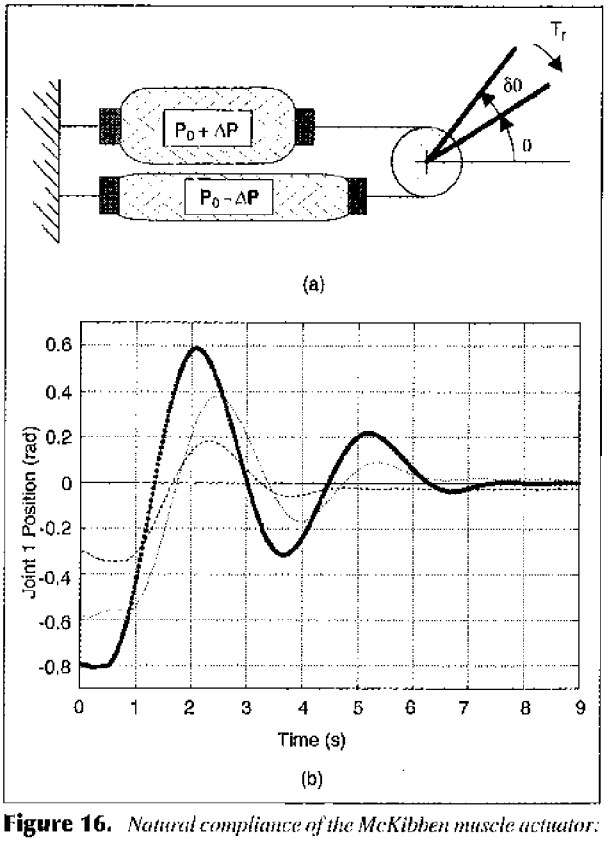

Figure 16. *Natural compliance of the McKibben muscle actuator: (a) the spiral spring nature of the McKibben muscle actuator; (b) open-loop response of the actuator (the curves represent the responses obtained after release for different $\delta\theta$ values).*

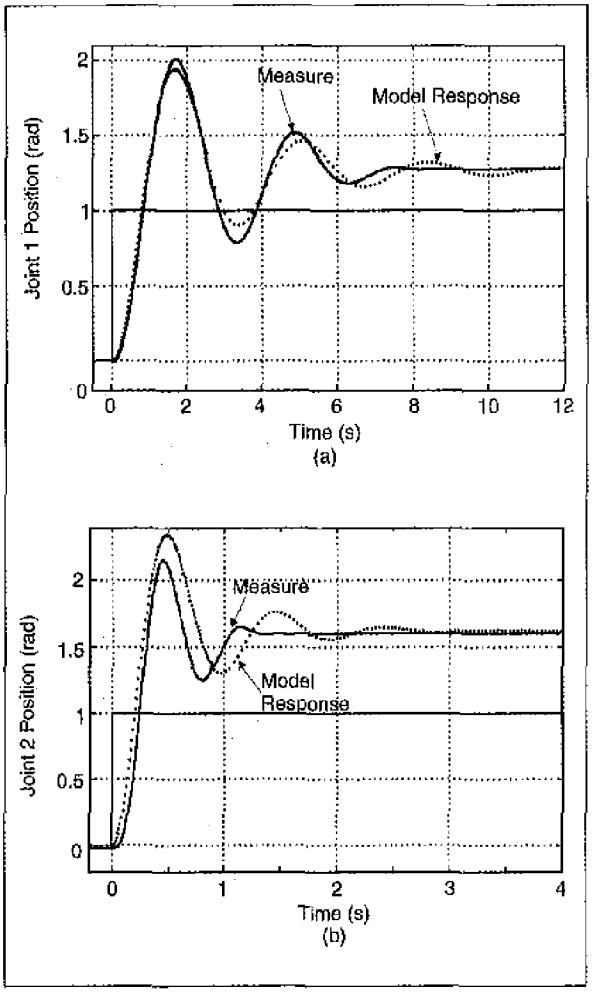

Figure 17. *Identification of the actuator system: (a) joint 1 of the 2-DOF robot arm; (b) joint 2 of the 2-DOF robot arm.*

I/P converters are removed, the McKibben muscle actuator is well adapted for driving powerful, compact, light, and compliant robot arms.

Dimensioning of the McKibben muscle actuator for maximum torque and size can be performed either by adjusting both initial radius r_0 and initial braid angle α_0 or the driving sprocket diameter R. Because the McKibben muscle maximum force is globally independent of the initial muscle length, for the same actuator power, the joint range can be tuned by modifying the initial muscle length l_0. From the basic actuator scheme of Fig. 13, it is easy to deduce that the McKibben muscle actuator joint range is $[-\varepsilon_0 l_0 / R$ (rad), $+\varepsilon_0 l_0 / R$ (rad)]. Using the parameter R, the designer can find a compromise between the actuator maximum torque and its joint range. From (21), it is easy to deduce that the maximum torque is obtained for $\theta = 0$ and $\Delta P = \Delta P_{max}$. If we denote as P_{max} the maximum actuator working pressure (typically 5 or 6 bar), and if P_0 is chosen equal to $P_{max} / 2$, ΔP_{max} will be equal to $P_{max} / 2$, which leads to a maximum torque equal to

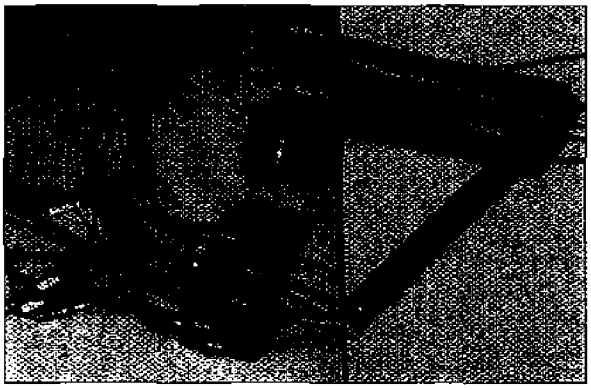

Figure 18. *Two-DOF SCARA-type robot arm prototype actuated by McKibben muscles.*

$(k_1 P_{max} / 2)$. The weak value of the parameter ε_0 (imposed by the fact that $2\varepsilon_0$ cannot exceed the maximum muscle contraction ratio of about 30%), however, implies choosing relatively high initial muscle lengths for joints with high angular ranges. This point is certainly the most negative compared with traditional electrical or hydraulic robot actuators. The rotation axis being perpendicular to the "muscle plane," however, facilitates integration of the muscles longitudinally inside the robot links, in the same way that natural muscles are set in our limbs.

The 2-DOF SCARA-type robot arm prototype shown in Fig. 18 has been designed in the laboratory [36]. It is actuated by two pairs of identical muscles of parameters $l_0 = 34$ cm, $r_0 = 0.7$ cm, and $\alpha_0 = 23°$. The two axes of the robot are directly driven by sprockets with a radius of 1.5 cm. The choice for $\varepsilon_0 = 10\%$ leads to a joint range of ± 2.2 rad ($\pm 130°$). The maximum torque is about 7 N·m. Both robot links are 40 cm long, which gives the robot an 80-cm span comparable to that of the Adept one SCARA robot. The two pairs of muscles are inserted in the first link, which weighs about 4 kg. The second link weighs only about 0.6 kg to facilitate the contact for the tool with its environment.

Control of Robot Arms Actuated by McKibben Muscle Actuators

Problem Position

The open-loop control of the antagonistic McKibben muscle actuator joint position makes possible the simple open-loop control of McKibben muscle robots. Due to the high actuator nonlinearities, however, this approach requires supervising of the robot task. In the case of automatic tasks, interesting programming experiments have been developed by applying a neural network to a 5-DOF Soft-Arm supervised by external cameras [37]. A Kohonen-type neural network has been used to position the robot end-effector within 1 cm of its desired position after learning. Learning sessions are very time consuming (i.e., several hours), and positioning trials take approximately 30 s. Recently, the au-

thors have developed a feedforward neural network controller, using robot joint data and corresponding measured pressure, to learn a specified joint trajectory [38]. After a training session of a few minutes, a joint tracking accuracy between 0.1 and 1° is obtained. In the case of teleoperated tasks, the operator can play the part of supervisor. The McKibben muscle pressure sensitivity and the response time of its contraction are well suited to the direct interaction of the McKibben muscle robot with the human operator, as Bridgestone's engineers proved by designing a Soft-Arm devoted to those with disabilities.

For widespread use of these actuators in the field of arm robotics, however, quick and accurate control of the McKibben muscle actuator is required. Within this framework, several research works have been concerned with the development of closed-loop control of McKibben muscle robots. Having tested a feedforward+PID-type controller approach [39], Caldwell and his team are turning to an adaptive controller [40]. The latter was applied to an actuator composed of two antagonistic McKibben muscles, although only the flexor is used for controlling the motion, with the extensor being used as a return spring. A passive muscle instead of an active antagonistic McKibben muscle limits the actuator capabilities. Therefore, the authors then considered a true antagonistic McKibben muscle actuator for which the adaptive pole placement scheme discussed in [40] has been extended to the muscle couple [41]. The adaptive controller is based on the on-line identification of a model with five parameters and three time delays. Recently, the authors have announced that the position regulation of the joints of their arm prototype is better than ±0.5° [42]. Furthermore, reasonable operation is achieved in less than 5 s and optimum operation in 30 s. One may wonder, however, whether the use of pneumatic valves by this team does not contribute to making the actuator model more complex (piezo-electric valves Hoerberger piezo 2000, 0.001 W per valve, switching at 40-50 Hz are used in [39]-[41] and high-speed MATRIX pneumatic valves operating at 100 Hz in [42]). I/P converters seem more relevant because their use leads to a simple off-line identification of the actuator system, as shown earlier. The identified model can then be integrated in the control as a linear feedforward term [43] or as a component of a nonlinear controller, as we will see in the discussion of our variable-structure control approach. Moreover, Caldwell's team does not consider the problem of controlling several joints together. Because of the direct-drive actuator principle, the joint control must be robust enough to support the dynamic variation of other robot joints. Cai and Yamaura's recent work has considered this problem in a study simulating the control of a 2-DOF robot actuated by McKibben muscles [44]. The simulation is based on a nonlinear empirical model of the McKibben muscle [45] completed by a classic dynamic robot model. A sliding-mode control approach was chosen because of its specific robustness and also because it is then possible to integrate a known model of the system, which contributes to global controller robustness. We can criticize this approach on two points. First, no pneumatic supply model is considered in the simulation. Second, it is well known that the complete dynamic model is difficult to run for robot arms of more than 2-DOF. The sliding-mode approach that we are now developing aims to overcome these difficulties and will be validated on a real robot arm.

Thus our model looks like the analogical form of N. Hogan's biological model in which the pressure variables play the part of biceps and triceps nervous controls. This comparison highlights the singularly anthropomorphic feature of the antagonistic McKibben muscle actuator.

Variable Structure Control of the Antagonistic McKibben Muscle Actuator

The variable-structure control based on the theory of variable-structure systems [46] is known to be particularly robust. The high-gain effect of its sliding-mode control suppresses the uncertainties due to parametric variations, external disturbances, and variable payloads. In the case of our actuator, we consider a desired joint trajectory $\theta_d(t)$, and the tracking error between the desired trajectory and the actual one, $\theta(t)$, is noted: $e = (\theta_d - \theta)$. The sliding mode is consequently associated with the switching line

$$S = Ce + \dot{e} = 0 \tag{26}$$

where C is a positive parameter. The equation of sliding mode is obtained by the equivalent control method proposed by Utkin [47]. According to this method, the control variable of our actuator ΔU will include its main component ΔU_{eq}, the so-called equivalent control, which corresponds to the ideal sliding mode, and its high-frequency discontinuous component v, which performs the oscillations around the sliding line according to the following basic equation:

$$\Delta U = \Delta U_{\text{eq}} + v. \tag{27}$$

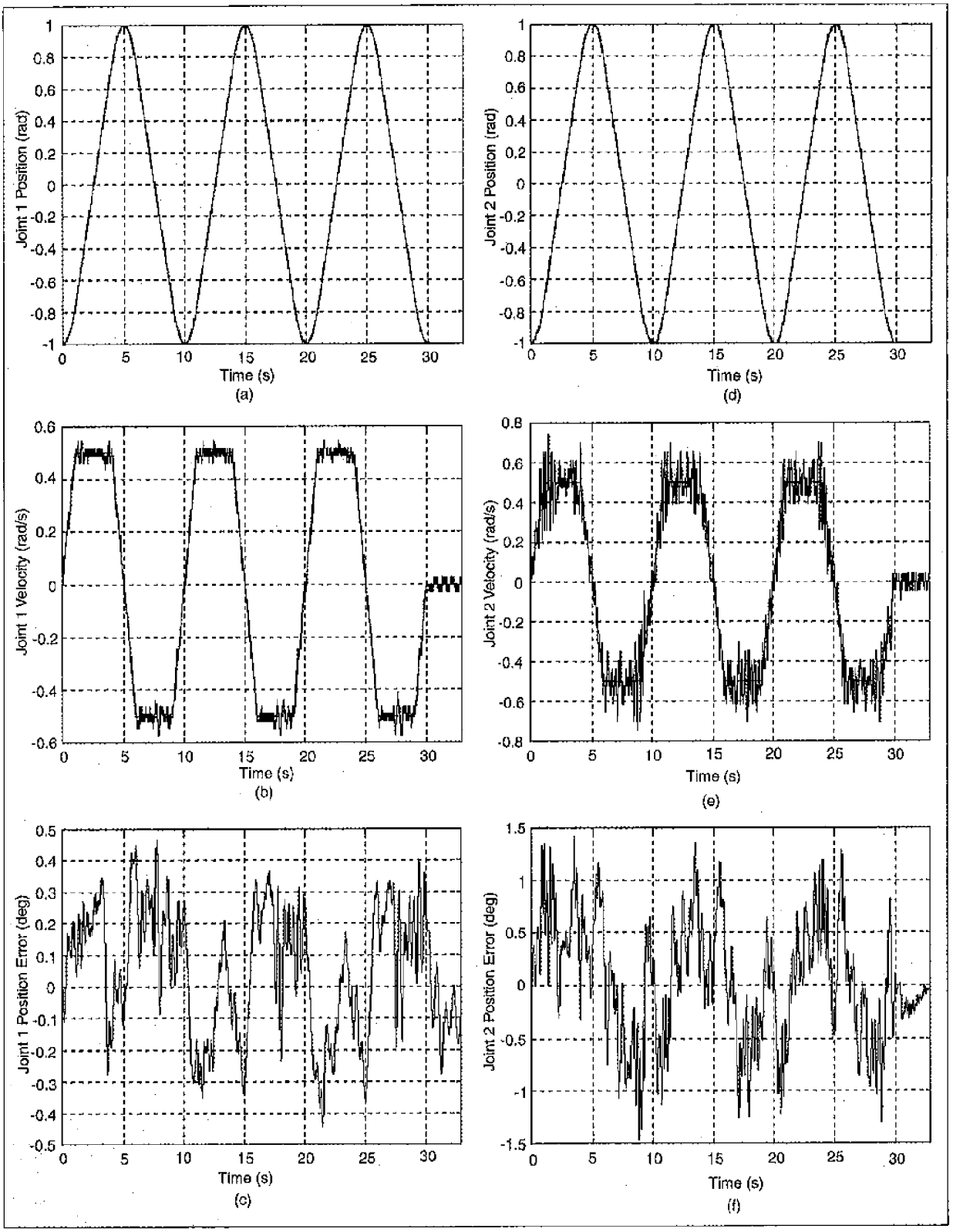

Figure 19. *Joint trajectory tracking of the two joints of the 2-DOF SCARA-type robot with McKibben artificial muscles, by variable structure control: (a), (b), (c) joint 1 case; (d), (e), (f) joint 2 case.*

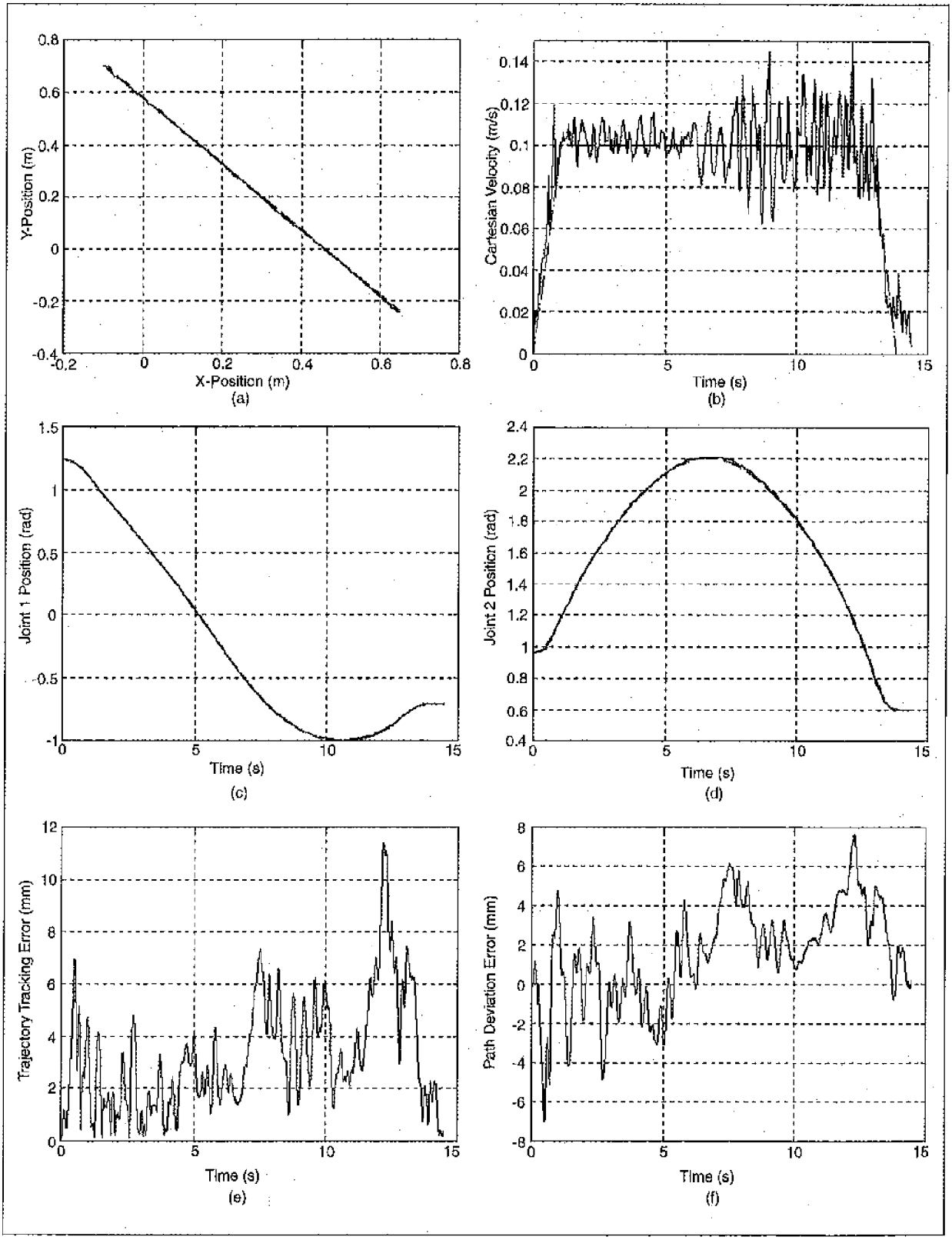

Figure 20. *Cartesian trajectory tracking of the 2-DOF robot-arm with McKibben artificial muscles, by variable structure control: (a), (b) Cartesian path and corresponding velocity profile; (c), (d) corresponding joint trajectories; (e), (f) corresponding evolution of trajectory tracking error and path deviation error.*

The equivalent control can be determined by assuming that the actuator behaves like the identified linear second-order system:

$$\ddot{\theta} + a_1\dot{\theta} + a_2\theta = b\Delta U_{eq}. \tag{28}$$

From the ideal sliding condition expressed by the algebric equation $\dot{S} = 0$, the equivalent control can be written as

$$\Delta U_{eq} = \frac{1}{b}\left[\left(\ddot{\theta}_d + a_1\dot{\theta}_d + a_2\theta_d\right) - a_2 e + (C - a_1)\dot{e}\right]. \tag{29}$$

This expression emphasizes the importance of the identified dynamic joint model applied to the desired trajectory, which plays the part of a feedforward-type term. Inserted in the equivalent control, the identified model contributes to the robustness of the control and "lightens" the nonlinear component of the controller. The discontinuous compo-

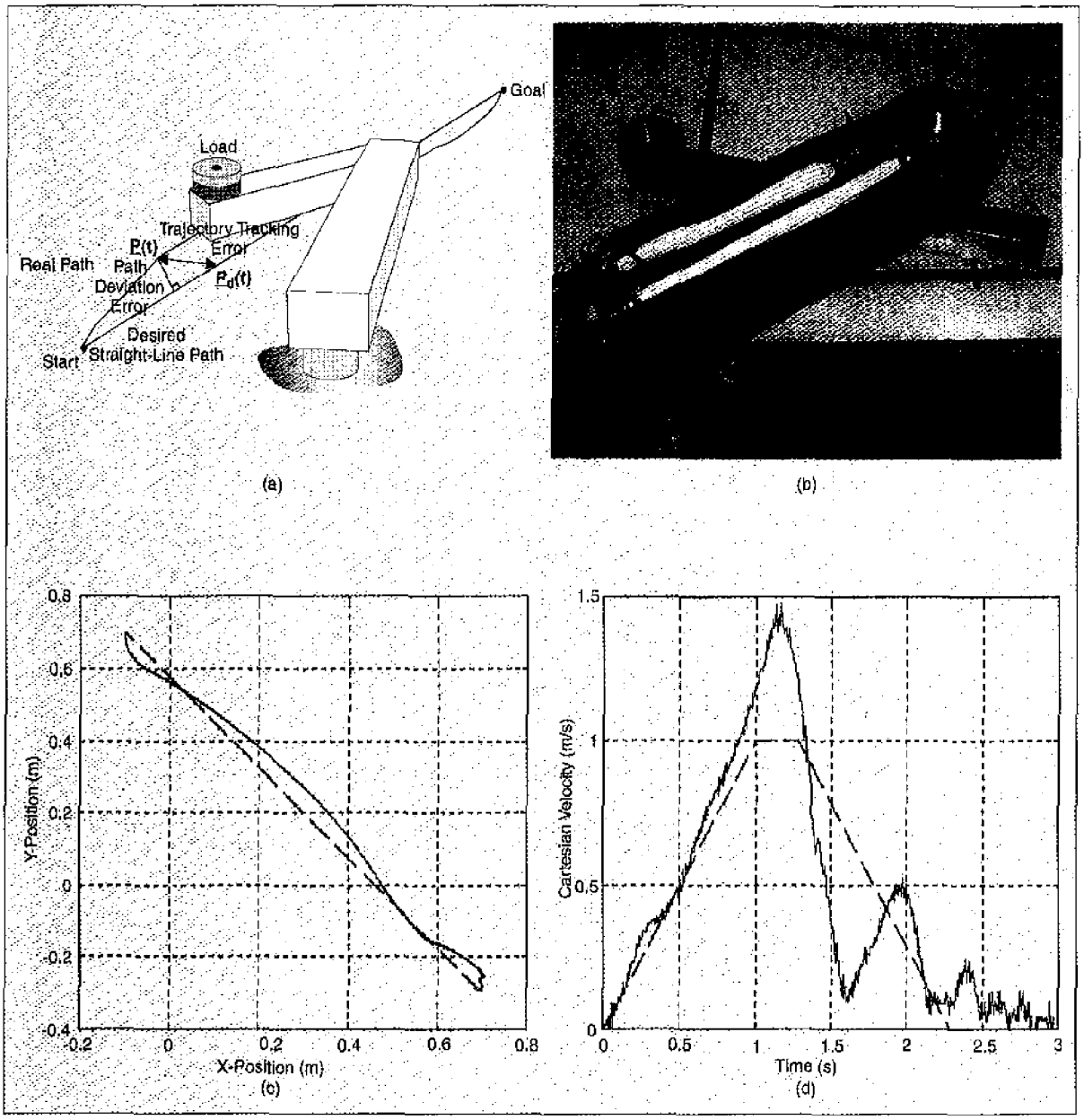

Figure 21. *Experimental robustness test of the 2-DOF SCARA-type robot arm with McKibben muscles controlled by variable structure: (a) criterion definition in Cartesian space; (b) loading of robot; (c), (d) results of Cartesian trajectory tracking reaching a 1-m/s cruising speed (with a 1-m/s^2 acceleration slope), with the robot extremity carrying a 1.5-kg load ("big" inertial variation case).*

nent has been chosen based on the the work by Harashima on the application of sliding-mode control to robot trajectory tracking [48]

$$v = (\alpha|e|+\beta|\dot{e}|+\gamma)\mathrm{sgn}(S). \tag{30}$$

Some improvements have been made to this basic control scheme:

- To avoid vibrations, it is preferable to make the sign change continuous by linearizing it;
- Oscillations around the sliding line can be limited by adding an acceleration term to the sliding line expression:

$$S = Ce + C'\dot{e} + C''\ddot{e} \tag{31}$$

while keeping the previous equivalent control expression. Because our system can be identified as second order, a weak sliding surface change is considered with $C'=1$ and C'' small (typically between 0.01 and 0.05 for C between 5 and 10);

- The discontinuous component v is saturated in a given range (±1 bar);
- As it is known that the static error is not equal to zero with variable structure control, an integrator term has been added to the controller, which is made active when the static error is smaller than a given limit (10°) while being saturated to a given value (± 0.8 bar).

Finally, the considered variable structure control has six main parameters which are C and C'' switching line parameters; α, β, λ discontinuous component parameters; and an integrator gain parameter. These parameters must satisfy the sliding condition $S\dot{S} < 0$. Their tuning can be based on a basic theoretical analysis of the sliding mode [49], and then fine-tuning can be performed experimentally. The control is simple enough to be sampled at high frequency (a sampling period of 2 ms has been considered in the experiments reported). Furthermore, because it uses an open-loop linear identified model of the actuator system, it can be fitted to each robot joint, as we have done for our 2-DOF SCARA-type robot.

Fig. 19 shows the application of the sliding-mode controller to the control of joint 1 and joint 2, considered separately, of our 2-DOF robot arm in the case of a joint trajectory tracking based on a pseudo-trapezoidal velocity profile defined by its cruising velocity and acceleration slope. Three to-and-fro motions have been programmed from −1 rad to +1 rad, with a cruising speed of 0.5 rad/s and an acceleration slope of 0.5 rad/s^2 [Fig. 19(a) and (b) and 19(d) and (e)]. By determining the position tracking error, the dynamic accuracy associated with the trajectory can be defined as the range of error e. In the case of joint 1, we get a ±0.5° dynamic accuracy [Fig. 19(c)], and in the case of joint 2, a ±1.5° dynamic accuracy [Fig. 19(f)]. A static joint accuracy of about ±0.2° can also be seen on these curves. The lower dynamic accuracy of joint 2 compared to joint 1 can be explained by its inertia being smaller than the joint 1 maximum inertia. Consequently, the joint 2 torque is more easily disturbed by the muscle dry friction. This fact limits application of the McKibben muscle actuator to the motorization of light robot links unless we can master muscle friction without losing its natural damping. This friction phenomenon also explains the deterioration of the dynamic accuracy when speed increases. The passage through zero of the muscle contraction speed occurring when the joint angle changes its sign indeed implies a transition between dry friction and kinetic friction with a cost in accuracy all the higher given that acceleration is high. In the case of the previous trajectory example, the dynamic accuracy is about ±1° for joint 1 and about ±3° for joint 2 when velocity and acceleration data are respectively equal to 1 rad/s and 1 rad/s^2, and it is about ±1.5° for joint 1 and about ±4° for joint 2 when velocity and acceleration data are respectively equal to 2 rad/s and 2 rad/s^2.

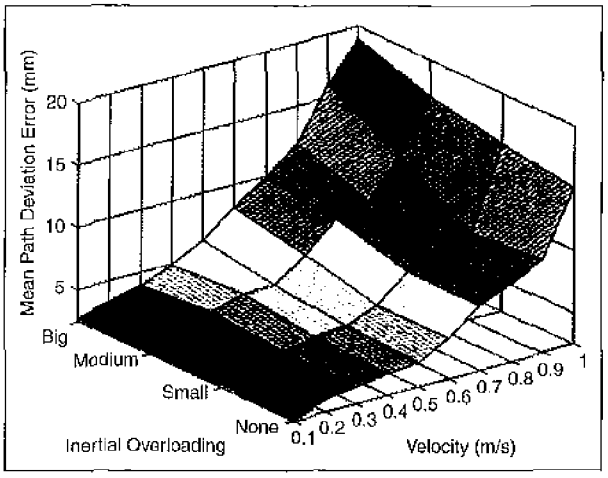

Figure 22. *Robustness graph giving the mean path deviation error as a function of velocity profile kinematic parameters and inertial overloading.*

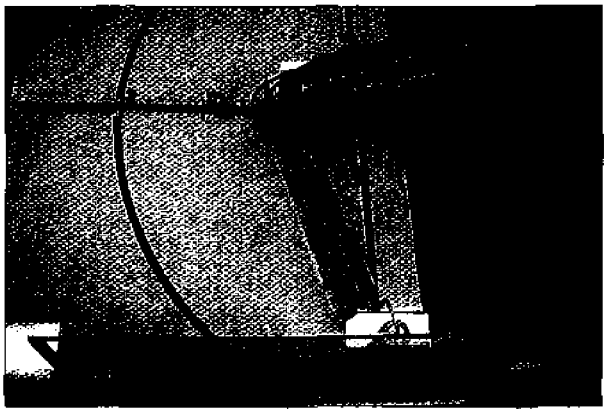

Figure 23. *Task example involving contact between the robot tool and a window pane, performed by the variable structure controller.*

Fig. 20 shows the application of the sliding-mode controller to trajectory tracking in Cartesian space. The trajectories considered are point-to-point straight lines performed according to a pseudo-trapezoidal velocity profile from which corresponding joint trajectories are determined by means of the SCARA-robot inverse kinematic model [50]. To quantify the dynamic accuracy in Cartesian space, a double criterion has been defined [Fig. 21(a)]. On the one hand, a Cartesian trajectory tracking error is defined as the norm of the vector from the desired Cartesian trajectory $\underline{P}_d(t)$ to the real one $\underline{P}(t)$ at each moment of the motion. On the other hand, in a more novel manner based on the straight-line nature of the considered trajectories, a path deviation error can be defined as the algebraic distance at each moment between the real path and the desired straight line. The second criterion is purely geometrical, whereas the first criterion takes into account both path and velocity profile deviation. The straight-line trajectory considered to test the robot controller has been chosen long enough from one side of the robot workspace to the other to characterize a mean dynamic accuracy. The Cartesian point [0,0] corresponds to the robot base and the X-axis to the line of the two links in the zero-joint configuration. The considered trajectory links point A [0.7 -0.3] to point B [-0.1 0.7] (coordinates given in meters). In the experiment reported in Fig. 20, a 0.1-m/s cruising linear velocity and a 0.1-m/s^2 linear acceleration have been considered. Fig. 20(a) gives the Cartesian space, Fig. 20(b) the actual velocity profile, Fig. 20(c) and (d) the corresponding joint trajectories, and Fig. 20(e) and (f) criterion evolutions. During Cartesian trajectory tracking, the joint 1 error remains in the range ±0.5°and the joint 2 error in the range ±1.5°. A mean path deviation error of 2.5 mm is obtained with a maximum error of 8 mm, and the mean trajectory tracking error is about 3.3 mm with a maximum error of 11 mm. On the curves in Fig. 20(e) and (f), error peaks correspond the velocity passing through zero for one or the other joint (at departure/arrival and when joint direction changes). We explain this phenomenon as due to the transient between the dry static and dry kinetic friction of the muscle thread.

While maintaining a globally cylindrical shape, the McKibben muscle produces a contraction force decreasing with its contraction ratio, as does skeletal muscle.

Robustness Test of the Variable Structure Controller Applied to the Antagonistic McKibben Muscle Actuator Robot Arm

The variable structure controller has been tested on the reference straight-line trajectory by varying velocity and acceleration data in the same ratio and loading the robot extremity, as shown in Fig. 21(b). When our robot is moving in the horizontal plane, this loading causes the inertial variation of each robot link. As we know the robot inertia matrix, we have considered three cases, in addition to the nonload case (denoted "none"); a load of about 500 g generating a 50% increase of maximum joint 1 inertia and 150% of joint 2 inertia (case denoted "small"); a load of about 1 kg, which doubles the previous inertial variations (case denoted "medium"); and an overload of about 1.5 kg, which trebles the inertial variations of the "small" case (case denoted "big"). Velocity and acceleration trajectory generator parameters vary from (0.1 m/s, 0.1 m/s^2) to (1 m/s, 1 m/s^2). Fig. 21(c) and (d) gives the result for a cruising velocity of 1 m/s (acceleration of 1 m/s^2) and the "big" inertial variation case.

Fig. 22 shows the 3-D evolution graph of the Cartesian dynamic accuracy in the form of the mean path variation error as a function of the velocity/acceleration parameter between 0.1 m/s-0.1 m/s^2 and 1 m/s-1 m/s^2 and of the four inertial variation cases considered. These experimental results show both the real power of the McKibben muscle actuator and the robustness of the sliding-mode control.

Moreover, the limited effect of the additive integral term enables using the sliding-mode controller for accurately performing a task involving contact between the robot and its environment without the help of any force sensor, as shown in Fig. 23. A straight-line trajectory has been programmed a few millimeters behind a vertically fixed window pane, and the natural compliance ensures the contact of a foam roller fixed at the robot end.

We have also compared this variable structure controller with a fuzzy controller consisting of a fuzzy PID based on a classic McVicar-Wheelan table [51]. Under the same experimental conditions, the fuzzy controller proves to be almost as robust as the variable structure controller; however, its fuzzy PID structure seems to be totally unadapted to the window-pane contact task example, because of the importance of the integral term, which results in losing the actuator natural compliance. If the integral component is indeed essential in the fuzzy controller, it is a small and secondary component in the variable structure controller because of the presence of the identified actuator model inside the control. This comparison highlights the superior robustness that can be expected of the artificial McKibben muscle actuator, which must combine a very high insensitivity to trajectory kinematic parameter variation for pick-and-place tasks and a certain insensitivity to joint deviation duration in tasks involving contact. By using the second-order actuator linear model, the variable structure controller proves to be superior to a fuzzy controller without any actuator

model to help the parametric robustness and consequently maintain the actuator natural compliance.

Conclusion

The McKibben artificial muscle is a pneumatic device characterized by its high level of functional analogy with human skeletal muscle. While maintaining a globally cylindrical shape, the McKibben muscle produces a contraction force decreasing with its contraction ratio, as does skeletal muscle. The maximum force-to-weight ratio can be surprisingly high for a limited radial dimension and for a conventional pressure range [0-6 bar]. A 50-g McKibben muscle can easily develop more than 1000 N under 5-bar pressure for an external radius varying from about 1.5 to 3 cm. Thus, robotics specialists are interested in this well-adapted artificial muscle for motorizing powerful yet compact robot arms. The basic McKibben muscle static modeling developed in this paper, which is based on the three main parameters (i.e., initial braid angle, initial muscle length, and initial muscle radius) and includes a three-parameter friction model of the thread against itself, has shown its efficiency in both isometric and isotonic contraction.

Two antagonistic McKibben muscles define a rotoid actuator that profits from the McKibben muscle power. The actuator has passive compliance, which results directly from the analogous nature of the McKibben muscle compared with skeletal muscle. We have termed this analogical property "natural compliance." Modeling of the actuator deduced from our simplified McKibben muscle model—without the considered friction model—shows that this "natural compliance" is based on a spiral spring-type restoring torque. The McKibben muscle actuator stiffness proves to be completed by natural damping that we have interpreted as the consequence of the kinetic friction produced by the muscle thread. Thus, although highly nonlinear, the McKibben muscle actuator can be approximated by a linear second-order system.

The natural compliance of the antagonistic McKibben muscle actuator, combined with its power and compactness, leads to a new kind of robot arm that more closely resembles the natural arm. Such robots can be applied to service robotics involving contact between the robot and its environment. Unlike industrial robots, however, no speed reducer can be used to maintain the actuator natural compliance. Therefore, a highly robust controller must be considered to address specific actuator nonlinearities and trajectory as well as load parameter variations. A variable structure controller has been tested on a 2-DOF SCARA-type robot prototype. In joint space, a static joint accuracy of about $\pm 0.2^\circ$ has been validated. Due to the nonlinearities of the robot, dynamic accuracy is dependent on experimental conditions in speed and link inertia driven by the actuator. A mean dynamic accuracy of $\pm 0.5^\circ$ has been obtained for a trapezoidal velocity profile of 0.5 rad/s cruising speed and a 0.5-rad/s^2 acceleration slope (joint 1 of our 2-DOF SCARA robot). If the link inertia is too weak, accuracy decreases under the same trajectory conditions because of the high level of actuator friction (joint 2 of our 2-DOF SCARA robot). In Cartesian space, a mean path deviation error between 3 and 6 mm has been validated on our 2-DOF SCARA robot moving over a speed range of 0.1 m/s to 0.5 m/s, with a maximum load of 1.5 kg (i.e., 30% of the weight of the robot's two links). The robustness of the variable-structure controller has been validated. Moreover, the presence of the identified linear model in the equivalent control limits the controller feedback effect, which preserves the actuator natural compliance, as demonstrated in a contact experiment with the robot tracking on a window pane.

Although the "soft" nature of the McKibben muscle actuator seems to limit its accuracy and repeatability compared with industrial robot performances, it is likely to adapt well to tasks at the moderate speed and accuracy required in service robotics. The relationship between the joint range and the initial length of the McKibben muscle actuator is a drawback, however, for the design of a wrist offering high joint ranges, such as PUMA robot-type wrists. Conversely, 3-DOF McKibben muscle wrists may exhibit limited joint ranges, such as in the human wrist. This disadvantage leads to an interest in designing robot arms that compensate the wrist joint limitations using the redundancy of the upper arm joints. Our 7-DOF anthropomorphic arm project [52], as well as that of Caldwell's team [42] or the more biological "anthroform arm" project of Hannaford's team [24], will help to better define the application field for McKibben muscle robots.

Acknowledgment

We acknowledge the anonymous referees for their help through their very pertinent remarks and proposals.

References

[1] "Artificial muscle," *Life*, pp. 87-88, Mar. 14, 1960.

[2] H.F. Schulte, "The characteristics of the McKibben artificial muscle," in *The Application of External Power in Prosthetics and Orthotics*, Appendix H, Publication 87. Washington, DC: National Academy of Sciences, 1961, pp. 94-115.

[3] V.L. Nickel, M.D.J. Perry, and A.L. Garret, "Development of useful function in the severely paralysed hand," *J. Bone Joint Surgery*, vol. 45-A, no. 5, pp. 933-952, 1963.

[4] T.J. Engen and L.F. Ottnat, "Upper extremity orthotics: A project report," *Orthopedic & Prosthetic Appliance J.*, pp. 112-127, 1967.

[5] M.M. Gavrilovic and M.R. Maric, "Positional servo-mechanism activated by artificial muscle," *Med. Biol. Eng.*, vol. 7, pp. 77-82, 1969.

[6] M. Matsushita, "Synthesis of rubber artificial muscle," *J. Soc. Instrum. Contr. Eng.*, vol. 7, no. 12, pp. 110-116, 1968 (in Japanese).

[7] F.P.W., "Rubber muscles take robotics one step further," *Rubber Develop.*, vol. 37, no. 4, pp. 117-119, 1984.

[8] K. Inoue, "Rubbertuators and applications for robots," in *Proc. 4th Int. Symp. on Robotics Research*, Cambridge, MA, 1988, pp. 57-63.

[9] Bridgestone Corporation, Tokyo, Japan, *Soft Arm ACFAS Robot System*, 1987.

[10] Bridgestone Corporation and Taicubo Engineering, Tokyo, Japan, *Soft Boy: Advanced Painting System Unit*, 1993.

[11] T. Noritsu, T. Tanaka, and T. Yamanaka, "Application of rubber artificial muscle manipulator as a rehabilitation robot," in *Proc. 5th IEEE Int. Workshop*

on Robot and Human Communication (RO-MAN'96), Tsukuba, Japan, 1996, pp. 112-117.
[12] R.T. Pack, J.L. Christopher Jr, and K. Kawamura, "A Rubbertuator-based structure-climbing inspection robot," in *Proc. 1997 IEEE Int. Conf. on Robotics and Automation*, Albuberque, NM, 1997, pp. 1869-1874.
[13] G.B. Immega, "ROMAC muscle powered robots," in *Proc. RI-SME Conf. Robotics Research*, Scottsdale, AZ, 1986, pp. 18-21.
[14] K. Suzumori, "Flexible microactuator," *Trans. Jpn. Soc. Mechan. Eng. (C)*, vol. 55-518, pp. 2547-2552, 1989 (in Japanese).
[15] Y. Tanaka and T. Okada, "Fundamental study of artificial muscle made of rubber," *Trans. Jpn. Soc. Mechan. Eng (C)*, vol. 58-545, pp. 217-224, 1992 (in Japanese).
[16] S.D. Prior and A.S. White, "Measurements and simulation of a pneumatic muscle actuator for a rehabilitation robot," *Simulation, Practice and Theory*, vol. 3, no. 2, pp. 81-117, 1995.
[17] S. Greenhill, "The digit muscle," *Indust. Robot*, vol. 20, no. 5, pp. 29-30, 1993.
[18] Shadow Robot Group (London), *The SHADOW Air Muscle*, http://www.shadow.org.uk/
[19] B. Hannaford, J.M. Winters, C-P. Chou, and P. Marbot, "The anthroform biorobotic arm: A system for the study of spinal circuits," *Ann. Biomed. Eng.*, vol. 23, pp. 399-408, 1995.
[20] C-P. Chou and B. Hannaford, "Study of human forearm posture maintenance with a physiologically based robotic arm and spinal level neural controller," *Biol. Cybernet.*, vol. 76, pp. 285-298, 1997.
[21] A. Thallemer and R. Riedmüller, "Hochelastische Kontraktionsschläuche Gewährleisten Stabilität einer Lufthalle," *Maschinenmarkt*, 12 May 1997 (in German).
[22] R. Maillot, "Tyre carcase construction," in *Technological Encyclopedia of Rubber Industry*, G. Genin and B. Morisson, Eds. Paris: Dunod, 1956, pp. 60-106, (in French).
[23] E.C. Woods, *Pneumatic Tyre Design*. Cambridge: Heffer, 1952.
[24] Biorobotics Laboratory (University of Washington), http://rcs.ee.washington.edu/BRL/.
[25] B. Tondu and P. Lopez, "Theory of an artificial pneumatic muscle and application to the modelling of McKibben artificial muscle," C.R.A.S., *French National Academy of Sciences*, Series IIb, vol. 320, pp. 105-114, 1995 (in French with an abridged English version).
[26] C-P. Chou and B. Hannaford, "Measurement and modeling of McKibben pneumatic artificial muscles," *IEEE Trans. Robot. Automat.*, vol.12, no.1, pp. 90-102, 1996.
[27] W.A. Nash, *Theory and Problems of Strength of Materials*. Schaum's Outline, New York: McGraw-Hill Inc., 1994.
[28] Samsom Corporation, Frankfurt, Electropneumatic Converter I/P 5288.
[29] B. Tondu and P. Lopez, "The McKibben Muscle and its use in actuating robot-arms showing similarities with human arm behaviour," *Indust. Robot*, vol. 24, no. 6, pp. 432-439, 1997.
[30] W.J. Roff, *Fibres, Plastics, and Rubbers, A Handbook of Common Polymer*. London: Butterworths Scientific, 1956.
[31] B. Armstrong-Hélouvry, *Control of Machines with Friction*. Kluwer, 1991.
[32] H.G. Howell, K.W. Mieszkis, and D. Tabor, *Friction in Textiles*. London: Butterworths Scientific, 1959.
[33] A. Sanchez, V. Mahout, and B. Tondu, "Nonlinear parametric identification of a McKibben pneumatic artificial muscle using flatness property of the system," in *Proc. 1998 IEEE Int. Conf. Control Applications*, Trieste, Italy, 1998, pp. 70-74.
[34] N. Hogan, "Adaptive control of mechanical impedance by coactivation of antagonistic muscles," *IEEE Trans. Automat. Contr.*, vol. AC-29, no. 8, pp. 681-690, 1984.
[35] C. Ghez, "Muscles: Effectors of the motor system," in *Principles of Neural Science*, E.R. Kandel, J. H Schwartz, T. M. Jessekk, Eds, Englewood Cliffs, NJ: Prentice-Hall, pp. 548-563, 1991.
[36] V. Boitier, "Design and control of a 2-DOF SCARA-type robot actuated by pneumatic artificial McKibben muscles," Ph.D. dissertation, INSA, Toulouse, France, Nov. 1996 (in French).
[37] T. Hesselroth, K. Sarkar, P. van der Smagt, and K. Schulten, "Neural network control of a pneumatic robot arm," *IEEE Trans. Syst., Man, Cybernet.*, vol. 24, no.1, pp. 28-37, 1994.
[38] P. van der Smagt, F. Groen, and K. Schulten, "Analysis and control of a Rubbertuator arm," *Biol. Cybernet.*, vol. 75, pp. 433-440, 1996.
[39] D.G. Caldwell, G.A. Medrano-Cerda, and M.J. Goodwin, "Braided pneumatic actuator control of a multi-jointed manipulator," in *Proc. IEEE Int. Conf. Systems, Man and Cybernetics*, Le Touquet, France, 1993, pp. 423-428.
[40] D.G. Caldwell, G.A. Medrano-Cerda, and M. Goodwin, "Control of pneumatic muscle actuators," *IEEE Contr. Syst. Mag.*, vol. 15, no.1, pp. 40-48, 1995.
[41] G.A. Medrano-Cerda, C.J. Bowler, and D.G. Caldwell, "Adaptive position control of antagonistic pneumatic muscle actuators," in *Proc. IEE/RSJ Int. Conf. Intelligent Robots and Systems, Human Robot Interaction and Cooperative Robots*, Pittsburgh, PA, 1995, pp. 378-383.
[42] C.J. Bowler, D.G. Caldwell, and G.A. Medrano-Cerda, "Pneumatic muscle actuators: Musculature for an anthropomorphic robot arm," in *Proc. IEE Colloqium on Actuator Technology: Current Practice and New Developments*, London, 1996, pp. 8/1-8/5.
[43] B. Tondu, V. Boitier, and P. Lopez, "Naturally compliant robot-arms actuated by McKibben artificial muscles," in *Proc. 1994 IEEE-SMC Conf.*, San Antonio, TX, 1994, pp. 2635-2640.
[44] D. Cai and H. Yamaura, "A VSS control method for a manipulator driven by an artificial muscle actuator," *Electron. Commun. Japan*, part 3, vol. 80, no. 3, pp. 55-63, 1997.
[45] T. Kagawa, T. Fujita, and T. Yamanaka, "Nonlinear model of artificial muscle," *Trans. SICE*, vol. 29, no. 10, pp. 1241-1243, 1993 (in Japanese).
[46] V.I. Utkin, "Variable structure systems with sliding modes," *IEEE Trans. Automat. Contr.*, vol. AC-22, no. 2, pp. 212-222, 1977.
[47] V.I. Utkin, "Equations of sliding mode in discontinuous systems I-II," *Automat. Remote Contr.*, pp. 1897-1907, 1971; pp. 211-219, 1972.
[48] F. Harashima, T. Ueshiba, and H. Haschimoto, "Sliding mode control for robotic manipulator," in *Proc. EPE Conf.*, Brussels, 1985, pp. 251-256.
[49] M. Hamerlain, B. Tondu, Ch. Mira, and P. Lopez, "Variable structure control for an actuator with artificial antagonistic muscles," in *Proc. IEEE Worshop on Variable Structure Control of Power Conversion Systems (VARSCON'91)*, Reno, NV, 1991, pp. 73-79.
[50] T. Yoshikawa, *Foundations of Robotics*. Cambridge, MA: MIT Press, 1990.
[51] D. Vial, "Fuzzy control of McKibben artificial muscles actuators for robot arms," Ph.D. dissertation, INSA, Toulouse, France, Dec. 1997 (in French).
[52] B. Tondu, A. Daldlé, M. Conscience, and S. Ippolito, "Design and simulation of a 7-DOF anthropomorphic arm actuated by McKibben artificial muscles," in *Proc. 7th IEEE Int. Workshop on Robot and Human Communication (RO-MAN'98)*, Takamastu, Japan, 1998, pp. 653-659.

Bertrand Tondu received the M.Eng. degree from the ENSEEIHT, Toulouse, France, in 1981 and Ph.D. degree in robotics from the University of Montpellier, France, in 1984. From 1985-1986 he was a postdoctoral fellow at Systems Laboratory of NRC, Ottawa, Canada. From 1986-1988 he was on the Comissariat à l'Energie Atomique, Fontenay-aux-Roses, France. He is currently professor of robotics at the Institut National de Sciences Appliquées, Toulouse, France. His interests include industrial robotics and development of artificial muscle actuators for the control of anthropomorphic robots.

Pierre Lopez received the Ph.D. degree in electronics from the University of Toulouse, France, in 1967. He is currently Professor Emeritus at the Institut National de Sciences Appliquées, Toulouse, France. His interests include nonlinear control of robot arms and development of chemico-mechanical artificial muscles.